Hard X-ray phase tomography for brain tissue imaging

Inauguraldissertation
zur
Erlangung der Würde eines Doktors der Philosophie
vorgelegt der
Philosophisch-Naturwissenschaftlichen Fakultät
der Universität Basel

von

Peter Thalmann
aus Bauma, ZH

2019

Genehmigt von der Philosophisch-Naturwissenschaftlichen Fakultät auf Antrag von:

Prof. Dr. Bert Müller, Fakultätsverantwortlicher
Prof. Dr. Sarah Köster, Korreferentin

Basel, den 17. Oktober 2017

Prof. Dr. Martin Spiess, Dekan

Contents

Summary

Phase tomography based on hard X-ray double-grating interferometry (XDGI) is a well-established imaging technique for the three-dimensional visualization of soft tissues, providing tomograms with superior contrast. The experimental setup contains a beam-splitter grating and an analyzer grating. Both gratings have to be placed and oriented with high precision for an optimized functioning of the interferometer. The analyzer grating can be omitted, if the detection unit allows a direct detection of the interference pattern. Such a setup is termed hard X-ray single-grating interferometer (XSGI). XSGI profits from easier handling, as only one grating needs to be aligned, and from the related cost reduction. But, more importantly than that, for the XSGI the spatial resolution is not limited by the period of the analyzer grating, and for equal photon flux, the number of detected photons is increased by a factor of about two. In the present thesis, a peripheral human nerve was embedded in paraffin. In order to compare the performance of XSGI and XDGI for medically relevant, low-absorbing specimens, for both modalities the specimen was measured at the facility Deutsches Elektronen-Synchrotron (DESY), using synchrotron radiation. Subsequently, the acquired tomograms were superimposed using rigid registration, i.e. one dataset was translated and rotated to best fit the other one. Both techniques allow resolving anatomical features of the nerve investigated, including epineurium, perineurium, and endoneurium. Whereas the XDGI data exhibit a better contrast-to-noise ratio, the XSGI tomogram shows an improved spatial resolution by a factor close to two. Thus, it can be concluded that XSGI is the preferred approach for the visualization of paraffin-embedded soft tissues.

Single-distance phase retrieval (SDPR) is a further phase-tomographic approach based on the free-space propagation of the transmitted X rays, and therefore does not require any additional X-ray optical elements. This method yields tomograms with superior spatial resolution. In this study, it is shown how the combination of SDPR and XDGI allows for a precise segmentation of a mouse brain tumor from its surrounding tissue. First, prominent ring artifacts had to be removed from the SDPR-tomogram, before the tomograms could be superimposed using a Helmet-Transformation, i.e. one dataset was translated, rotated, and isotropically scaled to best fit the other one. Finally, an appropriate clustering of the joint-histogram using a watershed transformation resulted in a precise tumor localization.
The usage of a multiscale Hessian-based filter allows for the segmentation of the vessel network from the surrounding tissue within a phase tomogram. In this thesis, the segmented blood vessels from a brain tumor were compared with the ones from the surrounding tissue. For the tumor investigated we could conclude: (i) the vessel density in the tumor is increased by a factor of two, (ii) the averaged radius of the tumor vessels is slightly larger, (iii) the longest vessels detected within the tumor were three times shorter, and (iv) tortuosity measures were also found to be increased for the case of the tumor. Such studies may help to qualitatively describe tumor

formation and thereby contribute to the development of successful strategies against cancer.

Zusammenfassung

Computertomographie mit einem Zweigitterinterferometer (XDGI) ist eine besonders leistungsfähige Methode, um Weichgewebe mit hohem Kontrast dreidimensional darzustellen. Ein solches Interferometer besteht aus einem Phasen- und einem Absorptionsgitter, die beide mit hoher Präzision platziert und ausgerichtet werden müssen. Auf das Absorptionsgitter kann verzichtet werden, wenn die Detektoreinheit das Interferenzmuster direkt auflösen kann. Einen solchen Aufbau nennt man dann Eingitterinterferometer (XSGI). XSGI ist nicht nur billiger und profitiert von einer leichteren Handhabung als XDGI - was viel wichtiger ist - ist, dass das räumliche Auflösungsvermögen beim XSGI nicht durch die Periode des Absorptionsgitters limitiert ist und dass bei gleichem Photonenfluss die Anzahl der detektierten Photonen ungefähr doppelt so gross ist. Für die vorliegende Studie wurde ein peripherer Nerv in Paraffin eingebettet. Um die Leistungsfähigkeit von XSGI und XDGI anhand dieser schwach absorbierenden, menschlichen Probe direkt zu vergleichen, wurde die Probe am Deutschen Elektronen-Synchrotron (DESY) mittels Synchrotronsstrahlung gemessen. Die erhaltenen Tomogramme wurden mittels einer starren Transformation im dreidimensionalen Raum so verschoben und gedreht, dass sie bestmöglich in Übereinstimmung miteinander sind. Beide dreidimensionalen Datensätze zeigen die charakteristische Anatomie der Probe u.a. das Epineurium, das Perineurium und das Endoneurium. Während XDGI einen etwas besseren Kontrast lieferte, war das räumliche Auflösungsvermögen bei der XSGI-Messung fast doppelt so gut. Deshalb sollte man für die Phasentomographie von in Paraffin eingebettetem Weichgewebe XSGI bevorzugen.

Eine weitere Methode der Phasentomographie nutzt nur die Ausbreitung der Röntgenstrahlen nach dem Durchdringen der Probe und benötigt deshalb keine weiteren röntgenoptische Elemente. Dieses Verfahren erzeugt Phasentomogramme mit sehr hoher räumlicher Auflösung. Für das Verfahren verwendet man in Anlehnung an den englischen Begriff “single-distance phase retrieval” die Abkürzung SDPR. Die vorliegende Arbeit zeigt, dass sich SDPR und XDGI kombinieren lassen, um einen Mäusegehirntumor von dem umliegenden Gewebe virtuell zu trennen. Dazu mussten zunächst in dem SDPR Datensatz die zahlreichen Ringartefakte entfernt werden, bevor die Tomogramme mittels einer Helmert-Transformation im dreidimensionalen Raum so verschoben, gedreht und skaliert werden konnten, dass sie bestmöglich in Übereinstimmung miteinander sind. Die geschickte Gruppierung des gemeinsamen Histogramms ermöglicht schliesslich die präzise Unterscheidung von gesundem und krankem Gewebe.
Die Verwendung eines sogenannten multiskalen Hesse-Filters erlaubt die Segmentierung von Blutgefässen in einem Phasentomogramm vom umliegenden Gehirngewebe. In der vorliegenden Arbeit wurden die segmentierten Blutgefässe eines Tumors mit denen des umliegenden Gewebes verglichen. Für den untersuchten Tumor konnten folgende Schlussfolgerungen gezogen werden: (i) die Blutgefässdichte ist im Tumor doppelt so gross, wie im gesunden Gewebe, (ii) die Kapillaren haben im Tumor

einen grösseren mittleren Durchmesser, und (iii) die Blutgefässe sind im Tumor gegenüber dem umgebenden gesunden Gewebe stärker gewunden. Derartige Studien können helfen, die Tumorbildung quantitativ zu beschreiben und dadurch bei der Entwicklung von Strategien zur erfolgreichen Krebsbehandlung mithelfen.

List of Publications

P. Thalmann, C. Bikis, M. D. Dominietto, G. Schulz, B. Müller, and S. E. Hieber, "*Comparing capillaries in healthy and cancerous tissues on the basis of hard X-ray phase tomography*", *to be submitted to Microvascular Research.*

P. Thalmann, C. Bikis, G. Schulz, M. D. Dominietto, A. Rack, G. Schweighauser, S. E. Hieber, and B. Müller, "*Multi-modal synchrotron radiation-based phase tomography for label-free brain imaging*", *to be submitted to Journal of Synchrotron Radiation.*

A. Khimchenko, G. Schulz, **P. Thalmann**, and B. Müller, "*Implementation of a double-grating interferometer for phase contrast computed tomography in a conventional system nanotom®m*", *Submitted to APL Bioengineering.*

P. Thalmann, C. Bikis, G. Schulz, P. Paleo, A. Mirone, A. Rack, and B Müller, "*Removing ring artefacts from synchrotron radiation-based hard X-ray tomography data*", Proceedings of SPIE, 10391, 1039114 (2017).

A. Khimchenko, C. Bikis, G. Schweighauser, J. Hench, A.-T. Joita-Pacureanuc, **P. Thalmann**, H. Deyhle, B. Osmani, N. Chicherova, S. E. Hieber, P. Cloetens, M. Müller-Gerbl, G. Schulz, and Bert Müller, "*Imaging cellular and subcellular structure of human brain tissue using micro computed tomography*", Proceedings of SPIE, 10391, 103910K (2017).

A. Khimchenko, G. Schulz, H. Deyhle, **P. Thalmann**, I. Zanette, M-C. Zdora, C. Bikis, A. Hipp, S. E. Hieber, G. Schweighauser, J. Hench, and B. Müller, "*X-ray micro-tomography for investigations of brain tissues on cellular level*", Proceedings of SPIE, 9967, 996703 (2017).

P. Thalmann, C. Bikis, A. Hipp, B. Müller, S. E. Hieber, and G. Schulz, "*Single and double grating-based X-ray microtomography using synchrotron radiation*", Applied Physics Letters, 110, 061103 (2017).

A. Schneider, **P. Thalmann**, S. Pezold, *S. E. Hieber, and *P. C. Cattin, "*Augmented reality assisted brain tumor extraction in mice* ", Lecture Notes in Computer Science, 9254, 255-264 (2015). *S. E. Hieber and P. C. Cattin shared last authorship

Publications not directly related to the present thesis

C. Bikis, L. Degrugillier, **P. Thalmann**, G. Schulz, B. Müller, S. E. Hieber, D. F. Kalbermatten, and S. Madduri, "*Three-dimensional imaging and analysis of entire peripheral nerves after repair and reconstruction*", *submitted to the Journal of Neuroscience Methods.*

C. Bikis, **P. Thalmann.**, L. Degrugillier, G. Schulz, B. Müller, D. F. Kalbermatten, S. Madduri, and S E. Hieber, "*Three-dimensional and non-destructive characterization of nerves inside conduits using laboratory-based micro computed tomography*", *submitted to the Journal of Neuroscience Methods.*

G. Schulz, C. Götz, M. Müller-Gerbl, I. Zanette, M-C. Zdora, A. Khimchenko, H. Deyhle, **P. Thalmann**, and B. Müller, "*Multimodal imaging of the human knee down to the cellular level*", Journal of Physics: Conference Series, 849, 012026 (2017).

A. Khimchenko, C. Bikis, G. Schulz, M-C. Zdora, I. Zanette, J. Vila-Comamala, G. Schweighauser, J. Hench, S. E. Hieber, H. Deyhle, **P. Thalmann**, and B. Müller, "*Hard X-ray submicrometer tomography of human brain tissue at Diamond Light Source*", Journal of Physics: Conference Series, 849, 012030 (2017).

C. Bikis, P. Janz, G. Schulz, G. Schweighauser, J. Hench, **P. Thalmann**, H. Deyhle, N. Chicherova, A. Rack, A. Khimchenko, S. E. Hieber, L. Mariani, C. A. Haas, and B. Müller, "*High-resolution synchrotron radiation-based phase tomography of the healthy and epileptic brain*", Proceedings of SPIE, 9967, 996706 (2017).

L-M. Botta, S. N. White, H. Deyhle, I. Dziadowiec, G. Schulz, **P. Thalmann**, and B. Müller, "*Comparing natural and artificial carious lesions in human crowns by means of conventional hard X-ray micro-tomography and two-dimensional X-ray scattering with synchrotron radiation*", Proceedings of SPIE, 9967, 99670S (2017).

H. Deyhle, G. Schulz, A. Khimchenko, C. Bikis, S. E. Hieber, C. Jaquiery, C. Kunz, M. Müller-Gerbl, S. Höchel, T. Saxer, A. K. Stalder, B. Ilgenstein, F. Beckmann, **P. Thalmann**, M. Buscema, N. Rohr, M. N. Holme, and B. Müller, "*Imaging tissues for biomedical research using the high-resolution micro-tomography system nanotom®m*", Proceedings of SPIE, 9967, 99670Q (2017).

S. E. Hieber, C. Bikis, A. Khimchenko, G. Schulz, H. Deyhle, **P. Thalmann**, N. Chicherova, A. Rack, M-C. Zdora, I. Zanette, G. Schweighauser, J. Hench, and B. Müller, "*Computational cell quantification in the human brain tissues based on hard X-ray phase-contrast tomograms* ", Proceedings of SPIE, 9967, 99670K (2017).

G. Schulz, C. Götz, H. Deyhle, M. Müller-Gerbl, I. Zanette, M-C. Zdora, A. Khimchenko, **P. Thalmann**, A. Rack, and B. Müller, "*Hierarchical imaging of the human knee*", Proceedings of SPIE, 9967, 99670R (2017).

A. Khimchenko, G. Schulz, I. Zanette, M.-C. Zdora, A. Hipp, H. Deyhle, S. E. Hieber, C. Bikis, G. Schweighauser, J. Hench, **P. Thalmann**, and B. Müller, "*Single grating X-ray phase-contrast tomography for evaluation of brain tissue degeneration on cellular level*", European Cells and Materials, 32 Supplement 2, 41 (2016).

H. Deyhle, I. Dziadowiec, L. Kind, **P. Thalmann**, G. Schulz, and B. Müller, "*Mineralization of early stage carious lesions in vitro - A quantitative approach*", Dentistry Journal, 3, 111–122 (2015).

H. Deyhle, **P. Thalmann**, I. Dziadowiec, F. Beckmann, G. Schulz, and B Müller, "*Micro computed tomography for the investigation of tooth hard tissues*", European Cells and Materials, 30 Supplement 1, 36 (2015).

M. D. Dominietto, **P. Thalmann**, S. Lang, S. E. Hieber, G. Schulz, and B. Müller, "*Texture and shape quantification to characterize angiogenesis in tumour tissue*", European Cells and Materials, 30 Supplement 1, 26 (2015).

W. Kuo, **P. Thalmann**, G. Schulz, A. Marmaras, E. P. Meyer, A. Lang, S. E. Hieber, U. Olgaç, B. Müller, and V. Kurtcuoglu, "*Comparing vascular casts of murine kidneys with and without tissue corrosion*", European Cells and Materials, 30 Supplement 1, 51 (2015).

P. Thalmann, A. K. Stalder, B. Ilgenstein, N. Chicherova, H. Deyhle, F. Beckmann, B. Müller, and S. E. Hieber, "*Combination of micro computed tomography and histology for the investigation of bone grafting*", European Cells and Materials, 30 Supplement 1, 67 (2015).

F. Beckmann, I. Dziadowiec, L. Lottermoser, **P. Thalmann**, J. Herzen, I. Greving, G. Schulz, S. E. Hieber, and B. Müller, "*High-energy microtomography using synchrotron radiation at PETRA III / DESY for the 3D characterization of caries lesions*", European Cells and Materials, 28 Supplement 6, 23 (2014).

M. Buscema, M. N. Holme, H. Deyhle, G. Schulz, R. Schmitz, **P. Thalmann**, S. E. Hieber, N. Chicherova, P. C. Cattin, F. Beckmann, J. Herzen, T. Weitkamp, T. Saxer, and B. Müller, "*Grating interferometry-based phase microtomography of atherosclerotic human arteries*", Proceedings of SPIE, 9212 , 921203 (2014).

S. E. Hieber, A. Khimchenko, C. Kelly, L. Mariani, **P. Thalmann**, G. Schulz, R. Schmitz, I. Greving, M. Dominietto, and B. Müller , "*Three-dimensional imaging of human hippocampal tissue using synchrotron radiation- and grating-based micro computed tomography* ", Proceedings of SPIE, 9212, 92120S (2014).

G. Schulz, M. Dominietto, Z. Kovacs, R. Schmitz, S. E. Hieber, **P. Thalmann**, F. Beckmann, and B. Müller, "*Tumors in murine brains studied by grating-based phase contrast microtomography*", Proceedings of SPIE, 9212, 92120Q (2014).

P. Thalmann, S. E. Hieber, G. Schulz, H. Deyhle, A. Khimchenko, V. Kurtcuoglu, U. Olgac, A. Marmaras, W. Kuo, E. P. Meyer, F. Beckmann, J. Herzen, S. Ehrbar, and B. Müller, "*Three-dimensional registration of synchrotron radiation-based micro-computed tomography images with advanced laboratory micro-computed tomography data from murine kidney casts*", Proceedings of SPIE, 9212, 92120Y (2014).

T. Bormann, B. Müller, M. Schinhammer, A. Kessler, **P. Thalmann**, and M. de Wild, "*Microstructure of selective laser melted nickel-titanium*", Materials Characterization, 94, 189202 (2014).

F. M. Weiss, X. Zhao, **P. Thalmann**, H. Deyhle, P. Urwyler, G. Kovacs, and B. Müller , "*Measuring the bending of asymmetric planar EAP structure* ", Proceedings of SPIE, 8687, 86871X (2013).

H. Cabrera, D. A. Zanin, L. G. De Pietro, Th. Michaels, **P. Thalmann**, U. Ramsperger, A. Vindigni, and D. Pescia, "*Scale invariance of a diodelike tunnel junction*", Physical Review B, 87, 115436 (2013).

1 Introduction

Primary brain tumors are relatively uncommon, but they are associated with high morbidity and mortality. In children and young adults, they are responsible for approximately one out of three and one out of five cancer deaths, respectively, being tied with leukemia as the most common causes of cancer death. In addition, long-term consequences for children brain tumor survivors are also very common [1]. Amongst the malignant primary brain tumors, glioblastoma (GBM) is the most common and it is up to date a devastating disease, with prognosis remaining especially poor. In detail, only one out of twenty patients with glioblastoma survives up to five years upon diagnosis [1].
GBM is a highly vascularized tumor, thus angiogenic factors play a prominent role in its onset and development. Amongst them, vascular endothelial growth factor (VEGF), a potent mitogen of the vascular endothelial cells, has been studied extensively. Several current therapeutic approaches targeting GBM have been focused on VEGF-targeting and manipulation [2]. Nevertheless, bevazicumab, a monoclonal anti-VEGF-A antibody that is used as adjuvant tumor therapy with some clinical results in GBM, has not yielded a consistent effect on overall survival and several questions on its efficacy and proposed use as a tumor adjuvant therapy remain open [3, 4].
It is important to note, however, that even if the idea of anti-angiogenesis as a therapeutic approach for tumor treatment in general is at least half a century old [1], our present understanding on the field remains limited. VEGF, the most promising anti-angiogenic target to day, with good experience as adjuvant therapy [2], is considered to only play a major role for two out of the at least six tumor vessel categories. Given that out of these categories, four are not at all present in healthy tissue, there is need for a better understanding of angiogenesis, both at a molecular level, but also at the level of the vascular micro-anatomy of tumor and healthy tissue.
Furthermore, due to the intrinsic tumor heterogeneity that arises at a genetic level and is passed down to molecular, anatomical and microvascular level, the visualization of the entire vascular network is essential for the investigation of tumors [1,2]. Tumors are usually investigated by histology. The micrographs obtained by optical microscopy provide sub-micrometer resolution with reasonable contrast depending on the staining used, while immunohistochemistry also allows for the investigation of tissue functionality. However, histology does not provide true isotropic three-dimensional (3D) information, and can only be extended to the third dimension by means of serial sectioning. This is a time-consuming procedure, requiring specialized personnel and induces tissue deformation, such that difficult, non-rigid registration is required for the generation of a three-dimensional volume [5]. Other techniques such as magnetic resonance imaging (MRI) or conventional computed tomography (CT) do not fulfill the requirements due to insufficient spatial resolution or weak contrast.

Given the aforementioned requirements, synchrotron radiation-based micro computed tomography (SRμCT) has proven itself to be a suitable imaging technique for the visualization of a complete vascular network with a resolution able to resolve even the smallest capillaries [6, 7]. However, both studies used contrast agents such as staining or corrosion casts to achieve sufficient contrast. Nevertheless, in order to reduce systematic errors due to tissue preparation, a label-free imaging that better reflects the situation prior to specimen extraction should be the long-term goal. First investigations showed the potential of using SRμCT in phase-contrast mode to achieve a label-free imaging of brain tissue [8, 9] avoiding the usage of contrast agents, the associated leaking problems and the systematic errors introduced by tedious specimen preparation.
The propagation of light through a medium can be described by the refractive index

$$n(x, y, z) = 1 - \delta(x, y, z) + i\beta(x, y, z), \tag{1.1}$$

where δ, the refractive index decrement, accounts for the phase shift and β accounts for the attenuation of the wave, respectively [10]. For a single-component material and for photon energies far from absorption edges

$$\beta = \frac{\rho_a \sigma_a}{2k} = 0.01[barn]\rho_a k_0^3 \left(\frac{Z}{k}\right)^4, \tag{1.2}$$

$$\delta = \frac{\rho_a p}{k} = \frac{2\pi \rho_a Z r_e}{k^2}, \tag{1.3}$$

where ρ_a is the atomic number density, σ_a the absorption cross section, p the phase shift cross section, Z the atomic number, k the length of the wave vector, k_0 the length of a wave vector with wavelength of 1 Å, and r_e the classical electron radius, also known as the Thomson scattering length. Thus, for materials consisting of low-Z elements, such as brain tissue, the total phase shift cross section for hard X rays is about three orders of magnitude higher than the total absorption cross section [11–13], making phase tomography the preferential modality for the investigation of low-absorbing material.
The pioneer work for X-ray phase imaging was presented in 1965 by Bonse and Hart. The basic idea of the presented interferometer is, that the first part of the crystal acts as a beam splitter, the second part as two transmission mirrors and the third part as analyzer crystal. The presented crystal interferometer, was capable to acquire a Moiré pattern and induced phase shifts by introducing a lucite wedge. X-ray crystal interferometry is considered to be the most sensitive technique for phase shift detection, however, the field of view of the interferometer is limited by the diameter of the crystal ingot from which the interferometer is fabricated [14]. Nowadays, five decades later, there exists a variety of methods for the phase retrieval and its application for computed tomography for the imaging of soft tissues, such as X-ray double-grating interferometry [9], holotomography and in-line single distance phase tomography [15], the usage of near-field speckles [16], and two-crystal interferometer [17], or single-shot edge illumination [18].
For the investigation of low-Z elements double-grating interferometry has shown to provide tomograms with superior contrast, also for the imaging of brain tissues [8, 9]. Besides, propagation-based techniques have the advantage of not requiring additional X-ray optical elements, and therefore are capable of providing images with increased spatial resolution, but lower contrast as for instance achieved with X-ray double-grating inteferometry [15, 19].

Double-grating phase-contrast µCT

This technique to recover the phase information is based on the Talbot effect. When a plane wave transverses a periodic diffraction grating, self-images of the grating are produced at distinct distances downstream [20, 21]. The grating interferometer usually consists of two gratings, g_1 the beamsplitter grating and g_2 the analyzer grating. For monochromatic parallel-beam illumination the self images occur at the fractional Talbot distances

$$D_n = n\frac{p_{1,e}^2}{2\lambda} \tag{1.4}$$

where λ denotes the wavelength of the incident plane wave. For phase gratings the self-images occur at odd fractional Talbot orders (n = 1, 3, 5, ...) and for absorption gratings at even fractional Talbot orders (n = 0, 2, 4, ...). The period of intensity modulation is given by

$$p_{1,e} = \frac{p_1}{\eta}, \text{ with } \begin{cases} \eta = 1 & \text{for absorption and } \pi/2\text{–shift gratings} \\ \eta = 2 & 1 \text{ for a } \pi\text{–shift gratings} \end{cases}$$

where p_1 is the period of the beam splitter grating. Introducing a specimen into the beam induces a modulation of the wavefront $\Phi(x, y)$, resulting in a refraction of the beam by an angle α, where

$$\alpha(x) = \frac{\lambda}{2\pi}\frac{\partial\Phi(x)}{\partial x} = \int_{-\infty}^{\infty}\frac{\partial\delta(x)}{\partial x}dz. \tag{1.5}$$

The angular deviation in the beam induces a transverse shift of the interference pattern, $S(x)$, at the location of the analyzer grating given by

$$S(x) = \frac{\lambda d}{g_2}\frac{\partial\Phi(x)}{\partial x}. \tag{1.6}$$

To recover the differential of the wavefront phase profile the phase-stepping approach used in visible-light interferometry is applied [22]. This technique achieves an electron density resolution, which is typically higher than 1 electron per nm^3 [9] and therefore provides images with high contrast even for a low-absorbing specimen, such as it is the case for brain tissues [8, 9].

Single-distance in-line phase-contrast µCT

The derivation of the conventional absorption contrast tomography reconstruction algorithm is based on geometrical optics and does therefore not incorporate the phase information of the electromagnetic waves. Therefore, in conventional absorption-contrast tomography the detector is brought as close as possible to the specimen, in order to minimize scattering effects. Towards this purpose, a decoherer can also be used.

In comparison, free-space propagation-based µCT uses these scattering effects to derive the local phase change within the specimen. Due to propagation distance, the recorded radiographs contain absorption and phase information, where under the condition of weak defocusing, the phase information can be interpreted as Laplacian of the phase of the wavefront after transmitting the sample [23]. Many approaches

have been developed to retrieve the phase information using, e.g, a single distance approach [24, 25] or holotomography [26]. In this thesis the phase retrieval was performed using the method derived by Paganin et al. [27]. The algorithm is based on the transport of intensity equation (TIE) for a paraxial, monochromatic beam

$$\nabla_\perp \cdot (I(\mathbf{r}_\perp, z)\nabla_\perp \varphi(\mathbf{r}_\perp, z)) = -\frac{2\pi}{\lambda}\frac{\partial}{\partial z} I(\mathbf{r}_\perp, z), \tag{1.7}$$

whre $I(\mathbf{r}_\perp, z)$ is the intensity, and $\varphi(\mathbf{r}_\perp, z)$ the phase of the beam, and the position vector $\mathbf{r}_\perp$ lies in the plane perpendicular to the optic axis z [28]. Assuming a weak-absorbing single-component specimen, in the near-field, the inverse problem can be solved by:

$$\varphi(\mathbf{r}_\perp, z = 0) = \frac{\delta}{2\beta} \log_e \left(\mathcal{F}^{-1}\left(\frac{\mathcal{F}\{I(\mathbf{r}_\perp, z = D)/I_0\}}{1 + \frac{D\lambda\delta|\mathbf{k}_\perp|^2}{4\pi\beta}} \right) \right), \tag{1.8}$$

where I_0 denotes the intensity of the incident radiation, D the specimen-detector distance, and $\mathcal{F}$ the Fourier transform [27]. Despite the assumption of a single-component material, the algorithm has proven itself to be also robust for multi-component materials and soft tissue in particular [15].

2 Results

2.1 Single and double grating-based microtomography using synchrotron radiation

So far commercially available detector modules were not large enough to detect the interference pattern from the beam-splitter grating for centimetre-sized specimens with micrometer resolution, such that the grating interferometer setup needed to consist of two gratings, whereby the second one acted as an analyzer grating. In this study, we make use of a newly available detector module, thus allowing for the direct detection of the interference patter for centimetre sized specimens. The XSGI profits from easier handling, as only one grating has to be aligned, and from the related cost reduction. More importantly, spatial resolution is not limited by the analyzer grating period, and for the same flux, the number of detected photons is increased by a factor of about two. In this study we present a quantitative comparison of the well-established XDGI and the not yet common XSGI. The biological specimen used for the measurement was a paraffin-embedded human peripheral nerve. Both data sets allowed identifying anatomical structures of the specimen. The XSGI showed a reduced contrast-to-noise ratio, but an improvement of the spatial resolution by a factor of about two, in comparison to XDGI.

Published in Journal of Applied Physics Letter

APPLIED PHYSICS LETTERS **110**, 061103 (2017)

Single and double grating-based X-ray microtomography using synchrotron radiation

P. Thalmann,[1] C. Bikis,[1] A. Hipp,[2] B. Müller,[1] S. E. Hieber,[1] and G. Schulz[1]
[1]*Biomaterials Science Center, University of Basel, 4123 Allschwil, Switzerland*
[2]*Institute of Materials Research, Helmholtz-Zentrum Geesthacht, 21502 Geesthacht, Germany*

(Received 3 November 2016; accepted 20 January 2017; published online 6 February 2017)

Hard X-ray phase contrast imaging techniques have become most suitable for the non-destructive three-dimensional visualization of soft tissues at the microscopic level. Among the hard X-ray grating interferometry methods, a single-grating approach (XSGI) has been implemented by simplifying the established double-grating interferometer (XDGI). We quantitatively compare the XSGI and XDGI tomograms of a human nerve and demonstrate that both techniques provide sufficient contrast to allow for the distinction of tissue types. The two-fold binned data show spatial resolution of (5.2 ± 0.6) μm and (10.7 ± 0.6) μm, respectively, underlying the performance of XSGI in soft tissue imaging. *Published by AIP Publishing.* [http://dx.doi.org/10.1063/1.4975679]

X-ray grating interferometry (XGI) is a phase contrast imaging technique with distinctive contrast for applications and future developments in materials science, biomedical engineering, and beyond. Using synchrotron radiation, X-ray double-grating interferometry (XDGI) is one of the most powerful techniques in current use, due to its superior contrast, despite generally providing inferior spatial resolution compared to in-line methods.[1,2] Since the pixel size of commercially available detector modules is generally larger than the features of the obtained interference pattern from the beam-splitter grating g_1, grating interferometers often consist of two gratings, whereby the second one acts as an analyzer grating g_2.[3] The spatial resolution of such a set-up is limited by the periodicity of the analyzer grating.[3] Thus, the X-ray single-grating interferometer (XSGI) profits from easier handling, as only one grating has to be aligned, and from the related cost reduction. Most importantly, spatial resolution is not limited by the analyzer grating period, and for the same flux, the number of detected photons is increased by a factor of about two. Several research teams have performed phase tomography with a single-grating setup, including the proof of principle study by Takeda *et al.*[4] The three-page letter belongs to the first publications in the field and shows the feasibility of the approach. The explanations are corroborated by preliminary synchrotron radiation-based experiments on a two-component polymer with a limited field of view (FOV) of 1.3 mm^2. The authors mention in their proof-of-principle study 8 μm spatial resolution and a 9 mg/cm^3 detection limit of density deviation. As the authors only briefly explained how the quantities were derived, one has to consider them as estimates. It remains unclear how the refractive index deviation was evaluated from the noise. Thus, the letter is in line with the communications of other teams.[5] Furthermore, due to the small FOV, both settings used do not allow for a tomography of a centimeter-sized biomedical specimen with the necessary resolution of a few micrometers within a reasonable acquisition time. So far, there exists no detailed study on the quantitative evaluation of the XSGI performance in comparison to a well-established X-ray imaging technique.

For tissues, which are mainly composed of low atomic number elements, the phase-shift cross-section for X-rays is about 10^3 times higher than for the related absorption.[6,7] Therefore, X-ray phase contrast techniques exhibit superior contrast between internal anatomical structures within soft tissues not seen in standard absorption techniques.[8] In particular, peripheral nerves are attractive, because numerous animal models for nerve regeneration are available, and these studies often lack appropriate three-dimensional imaging with true micrometer resolution.[9,10] The models often rely on bio-engineered scaffolds, and here, detailed microstructural knowledge allows for targeted modification of the scaffolds' properties and biocompatibility.[11] Recent studies indicate that hard X-ray micro computed tomography, especially with synchrotron radiation, is well-suited to solve imaging tasks for animal models.[12,13] For the present communication, a human peripheral nerve was chosen, as the preparation procedure is standard in pathology, while the spatial resolution necessary to make the nerve anatomy visible is less ambitious than for the rodent peripheral nerve. The purpose of the present study is to make a direct comparison between XSGI and XDGI while analyzing a human peripheral nerve, which necessarily has to include both spatial resolution and the contrast-to-noise ratio (CNR).

The tomography measurements were carried out at the beamline P07 (PETRA III, DESY, Hamburg, Germany), operated by the Helmholtz-Zentrum Geesthacht.[14] An undulator source, in combination with a double-crystal monochromator consisting of two Si(111) Laue crystals on Rowland geometry, was used. Photon energy was set to 40 keV with an estimated photon flux of around 6×10^{13} $\text{s}^{-1}\,\text{mm}^{-2}$.

XSGI measurement was performed using a beam-splitter grating with a periodicity of $p_1^{(s)} = 4.8$ μm and a Si structure height of 7 μm, in order to induce a phase shift of $\pi/2$ for the photon energy selected. This results in self-images of the beam-splitter grating with a periodicity $p_1^{(s)}$ and maximal contrast at the fractional Talbot distances

$$d_n(\pi/2) = n\frac{p_1^2}{2\lambda}, \tag{1}$$

where n denotes an odd integer and λ denotes the wavelength of the incoming photons.[15]

The XDGI measurement was performed using a beam-splitter grating $g_1^{(d)}$ with a periodicity of $p_1^{(d)} = 4.8\,\mu$m and a Si structure height of $14\,\mu$m, typically used to achieve a phase shift of π.[16,17] The gold lines of the analyzer grating $g_2^{(d)}$ had a structure height of $\sim 100\,\mu$m with a periodicity of $p_2^{(d)} = 2.4\,\mu$m, corresponding to a transmission of only about 8%. The set-up for the XDGI measurement induces an interference pattern with a period $p_1^{(d)}/2$ and maximal contrast at the fractional Talbot distances

$$d_n(\pi) = n\frac{p_1^2}{8\lambda}, \tag{2}$$

where n is an odd integer.[15]

For both methods, we acquired 900 projections over 360°. At each projection angle, five phase-step images over one period of the interference pattern were recorded. With an exposure time of 140 ms per phase-step, this resulted in a scan time of almost 4 h. During camera readout and movement of the mechanical stages, the beam shutter was closed, in order to avoid unnecessary irradiation on the sample. The radiographs were recorded using a camera manufactured at the Institute for Data Processing and Electronics (Karlsruhe Institute of Technology, Karlsruhe, Germany) with a CMOS chip (CMOSIS, Antwerp, Belgium), featuring a 20 Megapixel (5,120 × 3,840) resolution with 6.4 μm-sized square pixels and a 100 μm thick $CdWO_4$ scintillator as an imaging detector. Both measurements were performed using a magnification of five, resulting in an effective pixel length of 1.3 μm.

For an adequate comparison of the two measurement techniques, the signal for both techniques should be comparable. Due to the gratings chosen, the inter-distance of the phase grating $g_1^{(s)}$ and the camera (C) had to be twice the distance $\overline{g_1^{(d)} g_2^{(d)}}$.[18] In addition, similar relative visibility from its respective maximum was achieved by the condition

$$\overline{g_1^{(d)} g_2^{(d)}}_{relativeVisibility} = \overline{g_1^{(d)} g_2^{(d)}}_{maximalVisiblity} - s, \tag{3}$$

$$\overline{g_1^{(s)} C}_{relativeVisiblity} = \overline{g_1^{(s)} C}_{maximalVisiblity} + 4 \times s, \tag{4}$$

where s denotes the distance away from maximal visibility.[15] Therefore, the distance between $g_1^{(d)}$ and $g_2^{(d)}$ was 248 mm, close to the third fractional Talbot order, and the distance between $g_1^{(s)}$ and C was 496 mm, close to the first fractional Talbot order. For the synchrotron radiation source, visibility

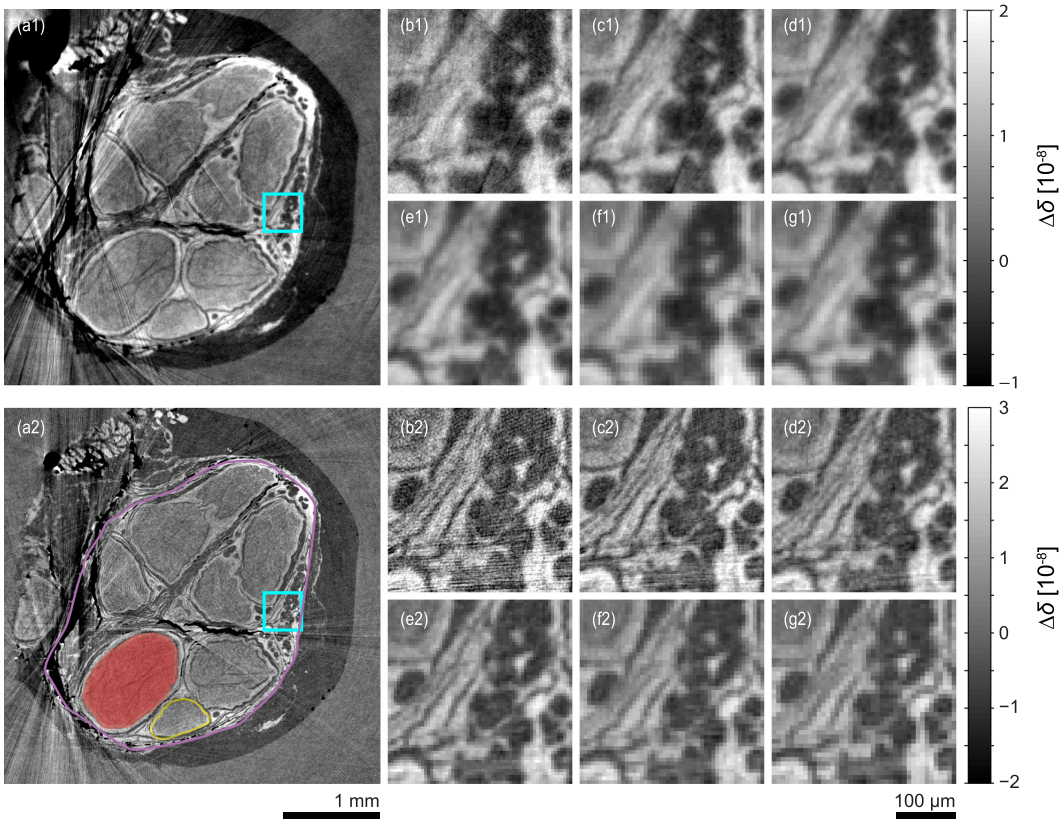

FIG. 1. X-ray phase tomography slice (a) of the human nerve using XDGI (top) and XSGI (bottom). The epineurium (violet), perineurium (yellow), and endoneurium (red) are clearly distinguishable for both techniques. The region enclosed by the cyan square is displayed for binning factors of 1 × 1 (b), 2 × 2 (c), 3 × 3 (d), 4 × 4 (e), 5 × 5 (f), and 6 × 6 (g). For both techniques, the grayscale bar was optimized for the respective figure displayed in (c), see also Fig. 2.

differences in the first fractional Talbot orders are negligible.[15]

The biological specimen used for the measurement was a human peripheral nerve, obtained post-mortem from a donated body. Informed consent for scientific use was obtained beforehand. All procedures were conducted in accordance with the Declaration of Helsinki and were approved by the Ethikkommission Nordwestschweiz. The peripheral nerve was extracted from the donated body and fixed in 4 % histological-grade buffered formalin. It was subsequently dehydrated and embedded in a paraffin/plastic polymer mixture, according to standard pathology procedure. The cylindrical sample for the tomography measurement was extracted from the paraffin block, using a metal punch with an inner diameter of 6 mm and was subsequently mounted on a specialized sample holder for the tomography data acquisition.

The phase-retrieved projections were achieved using a pixel-wise Fourier analysis. Then, the phase contrast tomograms were reconstructed using the standard filtered back-projection algorithm[19] implemented in Matlab® (2014a, The MathWorks, Inc., Natick, Massachusetts, USA) employing a modified filter kernel (Hilbert transform).[20] It has already been shown that the optimization of tomograms can be achieved using the optimized binning factor.[21] As we did not know this factor *a priori*, each dataset was reconstructed with the binning factors ($n \in \{1, ..., 6, 12\}$). We also verified that the sequence of the reconstruction process had no effect on the final results, by performing the binning at selected process steps along the reconstruction pipeline, namely, on the raw projections (only possible for XDGI), phase-retrieved images, and after integration. All three reconstruction sequences yielded almost identical results. Furthermore, we needed to account for the fact that the specimen was unmounted between the measurements. In detail, to compare the datasets for the applied binning factors, we performed rigid registration using a Powell optimizer and the Mattes mutual information metric. Translation registration was sufficient, since rotation invariance was assured by the mounting stage. For dataset resampling, we chose the nearest neighbor interpolator, so that the registration had no significant influence on the histogram of the floating image. Registration itself was performed using the library provided by ITK.[22]

Fig. 1 shows a characteristic slice of a human nerve provided by XDGI and XSGI, respectively. For both techniques, one can observe the main anatomical features of the nerve, wherein the epineurium, perineurium, and endoneurium are clearly distinguishable (see Fig. 1). Blood vessels are visible in the connective tissue, as well as nerve fascicles enclosed by the perineurium. The streak artefacts noticeable in both reconstructions originate from air-filled cracks in the paraffin. The XDGI images also contain prominent artefacts, due to air bubble formation during data acquisition. The most likely explanation is that the rougher paraffin surface allowed for the formation of micro air bubbles while inserting the specimen into the water tank, which then grow during irradiation. Therefore, smoothing of the paraffin reduces the artefacts from growing air bubbles at the paraffin surface.[23]

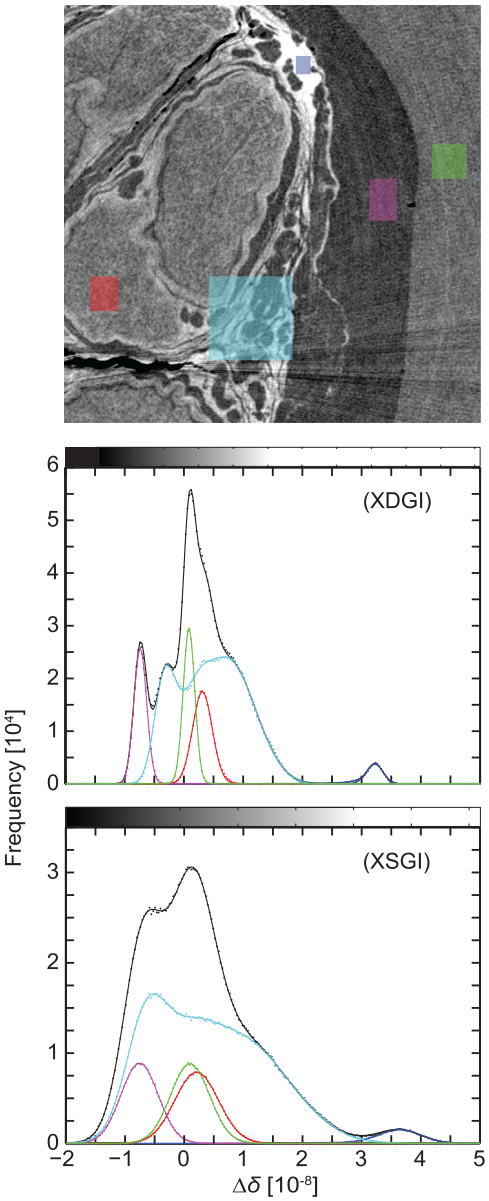

FIG. 2. Histogram for selected ROIs (top), water (green), paraffin (magenta), nerve fascicles with increased lipid composition (red), connective tissue (cyan), and connective tissue with increased formalin perfusion/dried out paraffin (blue) for XDGI (top) and XSGI (bottom), reconstructed with a binning factor of two. The corresponding histograms were fitted with Gaussians. The fitting parameters are listed in Table I and the resulting contrast-to-noise ratios are listed in Table II. The cyan curves' histograms belong to the zoom-ins in Fig. 1.

The histograms of the selected regions of interest (ROIs) of the XDGI and XSGI are shown in Fig. 2. The related mean and standard deviation values of the Gaussian distributions for selected tissues are listed in Table I. Quantitatively, we can define the contrast-to-noise ratio (CNR) for a specific feature as $|x_0^{feature} - x_0^{paraffin}|/\sigma_{paraffin}$, where x_0 denotes the

TABLE I. List of fitting parameters derived from the Gaussian fits in Fig. 2, where x_0 denotes the expectation value and σ^2 the variance of the $\Delta\delta$ values for different tissue types.

	XDGI		XSGI	
Tissue type	$x_0/10^{-8}$	$\sigma/10^{-8}$	$x_0/10^{-8}$	$\sigma/10^{-8}$
Preparation-affected connective tissue	3.22 ± 0.01	0.14 ± 0.01	3.63 ± 0.01	0.37 ± 0.01
Nerve fascicles	0.31 ± 0.01	0.16 ± 0.01	0.22 ± 0.01	0.37 ± 0.01
Water	0.09 ± 0.01	0.10 ± 0.01	0.10 ± 0.01	0.33 ± 0.01
Paraffin	−0.74 ± 0.01	0.11 ± 0.01	−0.75 ± 0.01	0.32 ± 0.01
Connective tissue I	0.76 ± 0.03	0.46 ± 0.02	0.93 ± 0.03	0.83 ± 0.02
Connective tissue II	0.15 ± 0.02	0.26 ± 0.03	0.03 ± 0.05	0.43 ± 0.04
Connective tissue III	−0.32 ± 0.01	0.17 ± 0.01	−0.65 ± 0.02	0.34 ± 0.01

expectation value of a homogeneous region and σ the corresponding standard deviation.[24] As the mean values of the peaks for both techniques are almost identical, the difference in contrast is predominantly given by the difference in the standard deviation of the paraffin peak. The findings illustrated in Fig. 3(a) show the power law dependence of the contrast-to-noise ratio on the binning factor, in comparison to the square dependence in standard absorption contrast.[21,25] The CNR was significantly lower for the XSGI, but this observed difference decreased when binning factors were increased. The selected results of the CNR analysis are listed in Table II.

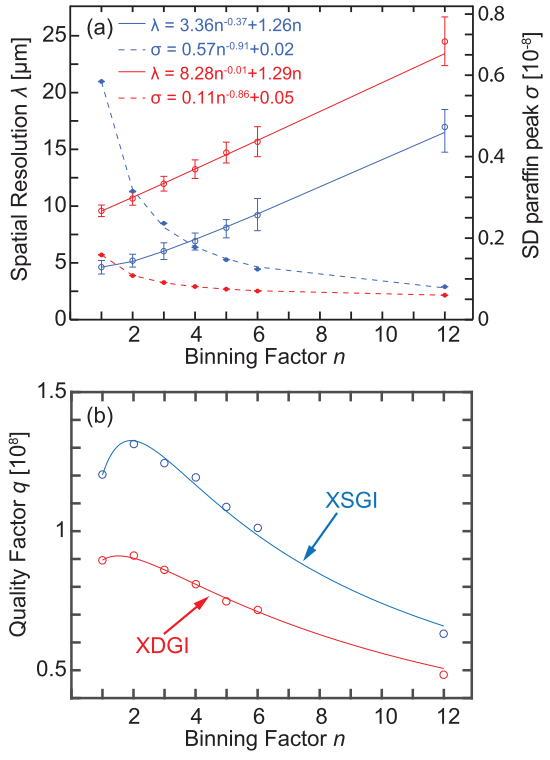

FIG. 3. (a) Spatial (dashed) and density (solid) resolution (standard deviation of the paraffin peak) versus binning factor. (b) Calculated dimensionless quality factor q versus binning factor. The fits were derived by using the fits from the upper figure. Both curves exhibit a maximum near a binning factor of two.

Spatial resolution can be defined as the intersection of the normalized modulation transfer function (MTF) with its 10 % value.[21] For the calculation, we have chosen a region at the paraffin-water interface, where the edge was almost parallel to the y-axis. In order to reduce noise effects, we applied the MTF to the median of the xz-plane over a height of around 50 μm. The results are plotted in Fig. 3(a) and confirm that XSGI provides images with higher resolution compared to ones acquired with XDGI. The spatial resolution of the XSGI was almost twice as high as that of the XDGI for the binning factors used.

Analogously to standard absorption contrast,[21] we can introduce the dimensionless quality factor $q = c \times 1/(\lambda \times \sigma^{1/3})$. For its calculation, we decided to take the paraffin width, similar to our approach to the CNR calculation, due to the homogeneity of the structure. The constant c follows directly from the proportionality of the decrement of the reflective index and the electron density, but was set to unity for the calculation of the quality factor. For both techniques, the quality factor reached its maximum for a binning factor of around two for the selected tissue (see Fig. 3(b)). From the approximate proportionality of the refractive index difference and the density difference, we received an estimation of the detection limit of the density deviation of (6.9 ± 0.7) mg/cm^3 for XDGI and (22.9 ± 0.7) mg/cm^3 for the XSGI for a binning factor of two.

In conclusion, we present in this study a quantitative comparison of the well-established XDGI and the not yet common XSGI. Despite the lower CNR of XSGI, the contrast was sufficient to identify the internal structure. Moreover, XSGI shows an improvement of the spatial resolution by a factor of about two. If the three times lower contrast in the unfiltered tomograms is sufficient for the investigation of the internal structure of the specimen, as it was in this study, XSGI is preferable to XDGI.

TABLE II. List of selected contrast-to-noise ratios calculated from the fitting parameters in Fig. 2.

	XDGI	XSGI
Water	7.55 ± 1.14	2.66 ± 0.15
Nerve fascicles	9.55 ± 1.26	3.03 ± 0.10
Affected connective tissue	36.00 ± 3.40	13.69 ± 0.43

The authors thank H. Deyhle, University of Basel, for his help with the measurements and many useful discussions, F. Beckmann, Helmholtz-Zentrum Geesthacht, for his help with the experimental set-up, as well as J. Hench and G. Schweighauser of the Neuropathology Department of the Basel University Hospital for providing the sample and helping with the special preparation required for tomography measurement.

The financial contribution of the Swiss National Science Foundation (Project Nos. 144535 and 147172) is gratefully acknowledged.

[1]I. Zanette, S. Lang, A. Rack, M. Dominietto, M. Langer, F. Pfeiffer, T. Weitkamp, and B. Müller, "Holotomography versus x-ray grating interferometry: A comparative study," Appl. Phys. Lett. **103**, 244105 (2013).
[2]S. Lang, I. Zanette, M. Dominietto, M. Langer, A. Rack, G. Schulz, G. Le Duc, C. David, J. Mohr, F. Pfeiffer, B. Müller, and T. Weitkamp, "Experimental comparison of grating- and propagation-based hard X-ray phase tomography of soft tissue," J. Appl. Phys. **116**, 154903 (2014).
[3]T. Weitkamp, A. Diaz, C. David, F. Pfeiffer, M. Stampanoni, P. Cloetens, and E. Ziegler, "X-ray phase imaging with a grating interferometer," Opt. Express **13**, 6296–6304 (2005).
[4]Y. Takeda, W. Yashiro, Y. Suzuki, S. Aoki, T. Hattori, and A. Momose, "X-ray phase imaging with single phase grating," Jpn. J. Appl. Phys. **46**, L89 (2007).
[5]M. Kagias, S. Cartier, Z. Wang, A. Bergamaschi, R. Dinapoli, A. Mozzanica, B. Schmitt, and M. Stampanoni, "Single shot x-ray phase contrast imaging using a direct conversion microstrip detector with single photon sensitivity," Appl. Phys. Lett. **108**, 234102 (2016).
[6]U. Bonse and F. Busch, "X-ray computed microtomography (μCT) using synchrotron radiation (SR)," Prog. Biophys. Mol. Biol. **65**, 133–169 (1996).
[7]A. Momose, T. Takeda, Y. Itai, and K. Hirano, "Phase-contrast X-ray computed tomography for observing biological soft tissues," Nat. Med. **2**, 473–475 (1996).
[8]G. Schulz, T. Weitkamp, I. Zanette, F. Pfeiffer, F. Beckmann, C. David, S. Rutishauser, E. Reznikova, and B. Müller, "High-resolution tomographic imaging of a human cerebellum: comparison of absorption and grating-based phase contrast," J. R. Soc., Interface. **7**, 1665–1676 (2010).
[9]S. Madduri, K. Feldman, T. Tervoort, M. Papalozos, and B. Gander, "Collagen nerve conduits releasing the neurotrophic factors gdnf and ngf," J. Controlled Release **143**, 168–174 (2010).
[10]H. Fujimaki, K. Uchida, G. Inoue, M. Miyagi, N. Nemoto, T. Saku, Y. Isobe, K. Inage, O. Matsushita, S. Yagishita, J. Sato, S. Takano, Y. Sakuma, S. Ohtori, K. Takahashi, and M. Takaso, "Oriented collagen tubes combined with basic fibroblast growth factor promote peripheral nerve regeneration in a 15 mm sciatic nerve defect rat model," J. Biomed. Mater. Res. A **105**, 8–14 (2017).
[11]B. M. Baker, A. O. Gee, R. B. Metter, A. S. Nathan, R. L. Marklein, J. A. Burdick, and R. L. Mauck, "The potential to improve cell infiltration in composite fiber-aligned electrospun scaffolds by the selective removal of sacrificial fibers," Biomaterials **29**, 2348–2358 (2008).
[12]M. Donnelley, K. S. Morgan, K. K. W. Siu, A. Fouras, N. R. Farrow, R. P. Carnibella, and D. W. Parsons, "Tracking extended mucociliary transport activity of individual deposited particles: longitudinal synchrotron X-ray imaging in live mice," J. Synchrotron Radiat. **21**, 768–773 (2014).
[13]R. P. Murrie, K. S. Morgan, A. Maksimenko, A. Fouras, D. M. Paganin, C. Hall, K. K. W. Siu, D. W. Parsons, and M. Donnelley, "Live small-animal X-ray lung velocimetry and lung micro-tomography at the australian synchrotron imaging and medical beamline," J. Synchrotron Radiat. **22**, 1049–1055 (2015).
[14]A. Hipp, F. Beckmann, P. Lytaev, I. Greving, L. Lottermoser, T. Dose, R. Kirchhof, H. Burmester, A. Schreyer, and J. Herzen, "Grating-based x-ray phase-contrast imaging at petra III," Proc. SPIE **9212**, 921206 (2014).
[15]T. Weitkamp, C. David, C. Kottler, O. Bunk, and F. Pfeiffer, "Tomography with grating interferometers at low-brilliance sources," Proc. SPIE **6318**, 63180S (2006).
[16]J. Herzen, T. Donath, F. Beckmann, M. Ogurreck, C. David, J. Mohr, F. Pfeiffer, and A. Schreyer, "X-ray grating interferometer for materials-science imaging at a low-coherent wiggler source," Rev. Sci. Instrum. **82**, 113711 (2011).
[17]M. Ruiz-Yaniz, I. Zanette, A. Sarapata, L. Birnbacher, M. Marschner, M. Chabior, M. Olbinado, F. Pfeiffer, and A. Rack, "Hard X-ray phase-contrast tomography of non-homogeneous specimens: grating interferometry *versus* propagation-based imaging," J. Synchrotron Radiat. **23**, 1202–1209 (2016).
[18]P. Modregger, B. R. Pinzer, T. Thüring, S. Rutishauser, C. David, and M. Stampanoni, "Sensitivity of X-ray grating interferometry," Opt. Express **19**, 18324–18338 (2011).
[19]A. C. Kak and M. Slaney, *Principles of Computerized Tomographic Imaging* (IEEE Press, 1988).
[20]F. Pfeiffer, O. Bunk, C. Kottler, and C. David, "Tomographic reconstruction of three-dimensional objects from hard X-ray differential phase contrast projection images," Nucl. Instrum. Methods Phys. Res., Sect. A **580**, 925–928 (2007).
[21]P. Thurner, F. Beckmann, and B. Müller, "An optimization procedure for spatial and density resolution in hard X-ray micro-computed tomography," Nucl. Instrum. Methods Phys. Res., Sect. B **225**, 599–603 (2004).
[22]See http://www.itk.org for The Insight Segmentation and Registration Toolkit (ITK), 2016.
[23]M. N. Holme, G. Schulz, H. Deyhle, T. Weitkamp, F. Beckmann, J. A. Lobrinus, F. Rikhtegar, V. Kurtcuoglu, I. Zanette, T. Saxer, and B. Müller, "Complementary x-ray tomography techniques for histology-validated 3d imaging of soft and hard tissues using plaque-containing blood vessels as examples," Nat. Protoc. **9**, 1401–1415 (2014).
[24]G. Schulz, T. Weitkamp, I. Zanette, F. Pfeiffer, M. Müller-Gerbl, C. David, and B. Müller, "Asymmetric rotational axis reconstruction of grating-based x-ray phase contrast tomography of the human cerebellum," Proc. SPIE **8506**, 850604 (2012).
[25]L. Grodzins, "Optimum energies for x-ray transmission tomography of small samples: Applications of synchrotron radiation to computerized tomography I," Nucl. Instrum. Methods Phys. Res. **206**, 541–545 (1983).

2.2 High-resolution brain tumor visualization using X-ray phase tomography

Already in 2007 Pfeiffer et al. [29] demonstrated that XDGI provides the necessary sensitivity for the identification of brain tumors in rats and the discrimination between white and gray matter in the cerebellum. And more recently, the complementarity of XDGI and SDPR phase tomography for the visualization of brain tumor specimens has been elucidated [15, 19]. We report in this study on advances in brain tumor imaging without the use of any contrast agent and with no need for tedious specimen preparation. A mouse brain tumor was measured ex-vivo after formalin fixation by means of XDGI and SDPR. Both techniques enabled us to visualize anatomical regions and features including, e.g., the hippocampal formation, thalamus, hypothalamus, ventricles, vessels and pia mater. The increased spatial resolution provided by SDPR even allowed for the detection of small capillaries and individual neurons. A post multi-model analysis allowed for a proper segmentation of the tumorous tissue by means of joint-histogram clustering and without the need of any sophisticated segmentation algorithm. In order to perform this measurement, we developed a tumor extraction tool using augmented reality [30] and an artefact removal protocol for high-resolution micro computed tomography.

To be submitted (target Journal of Synchrotron Radiation)

Multi-modal synchrotron radiation-based phase tomography for label-free brain imaging

Peter Thalmann,[a] Christos Bikis,[a] Georg Schulz,[a]* Marco D. Dominietto,[a] Alexander Rack,[b] Gabriel Schweighauser,[c] Simone E. Hieber[a] and Bert Müller[a]

[a] *Biomaterials Science Center, Department of Biomedical Engineering, University of Basel, 4123 Allschwil, Switzerland,* [b] *European Synchrotron Radiation Facilities (ESRF), Structure of Materials Group - ID19, 38000 Grenoble, France, and* [c] *Institute of Pathology, Department of Neuropathology, University Hospital of Basel, 4031 Basel, Switzerland. E-mail: georg.schulz@unibas.ch*

We report on advances in brain tumor imaging avoiding contrast agents and tedious specimen preparation. A mouse brain tumor was measured *ex vivo* after formalin fixation by means of synchrotron radiation-based hard X-ray single-distance in-line (SDPR) and double-grating (XDGI) phase tomography. Owing to an improved, two-step procedure for ring artefact removal, both techniques allowed for the discrimination between grey and white matter, as well as between healthy and cancerous tissues. Anatomical features were perceived, including the olfactory bulb, cortex, white matter tracts, ventricles, vessels and the pia mater. In addition, the increased spatial resolution provided by SDPR even allowed for the detection of smaller capillaries and individual neurons. Multi-modal post-analysis helped in properly segmenting the tumor by means of joint histogram clustering and without the need for a sophisticated segmentation algorithm. As both techniques are non-destructive, they allow for subsequent investigation of the specimens by standard histological analysis.

1. Introduction

Post-mortem brain tumor diagnosis and classification, for almost a century, has been entirely dependent on observations made with optical microscopes. Nevertheless, in 2016, the World Health Organization Classification of Tumors of the Central Nervous System was changed to incorporate recent developments in molecular diagnostics (Louis *et al.*, 2016). In this rapidly growing field, visualisation methods are being developed constantly, adapted and applied, for both brain tumor research and for clinical applications. The main reasons behind the need for additional, complementary visualisation methods are shortcomings in the gold standard itself, i.e. histology or electron microscopy, which are both two-dimensional approaches requiring staining or the use of more sophisticated probes and can only be extended to the third dimension by means of serial sectioning. This destructive process requires considerable time and technical expertise. Even when successful, serial sectioning provides considerably reduced resolution in the third dimension – usually ten times lower – with respect to its lateral resolution. In addition, the sectioning process itself deforms the tissue, such that difficult, non-rigid registration is required for the generation of a three-dimensional volume (Germann *et al.*, 2008; Schulz *et al.*, 2010*a*).

In contrast, X-ray tomography is a well-established technique that reflects the *in vivo* situation, providing images with isotropic voxel size and true micrometre resolution for centimetre-sized specimens. While common absorption-contrast technique yields only limited contrast for non-stained brain tissues (Schulz *et al.*, 2010*b*), for photon energies $\geq$10 keV, and far from any absorption edges, the total phase-scattering cross-section for tissues of low atomic number can be three orders of magnitude higher than the total absorption cross-section (Bonse & Busch, 1996; Momose, 2002; Als-Nielson & McMorrow, 2011) making phase tomography preferential for the investigation of brain tissue. Based on this fact, Pfeiffer *et al.* (2007*a*) demonstrated that double grating-based phase tomography (XDGI) provides the necessary sensitivity for identifying brain tumors in rats and differentiating between white and grey matter in the cerebellum. More recently, the complementarity of grating- and in line-based (SDPR) phase tomography for visualising tumor specimens has been elucidated (Lang *et al.*, 2014; Zanette *et al.*, 2013).

In this post-mortem study, we employ phase tomography to visualise a brain tumor, intentionally grown in a mouse brain, with the surrounding healthy tissues avoiding the application of contrast agents. We report on advances in multi-modal phase tomography using XDGI and SDPR. In detail, we demonstrate the improvement with respect to spatial resolution achieved by using SDRP, even allowing for the detection of small- to medium-sized neurons. Furthermore, we show that the lack of contrast often reported (Lang *et al.*, 2014; Huang *et al.*, 2015), to some extent, is a result of the high spatial resolution achieved and can therefore be improved by binning the radiographs (Thurner *et al.*, 2004). Especially interesting is that the registration of the phase tomography datasets leads to improved tumor segmentation by means of joint histogram clustering.

2. Materials and methods

2.1. Sample Preparation

One nude mouse (CD-1-Foxn1nu, Charles River Laboratories, France) eight weeks of age, weighting 24 g was used for the experiment. Murine glioma cells (GL261 cells) were implanted into the right frontal lobe, using a stereotactic frame for head fixation. *In vivo* magnetic resonance experiments were performed, using a PharmaScan 47/16 MRI system equipped with a 4.7 T magnet with a 16 cm bore diameter and a cryogenic quadrature RF surface transmit/receive coil (Bruker BioSpin Ettlingen, Germany). During the *in vivo* experiments, the animal was placed on a customised support equipped with a stereotactic system for head fixation and a face mask for anaesthetic administration (isofluorane 1.5 % to 2 %). A cannula for the administration of the contrast agent was inserted into the right tail vein. All the experiments were performed in strict adherence with Swiss law for animal protection and were approved by the local authorities (license ZH 168/2010). The mouse was sacrificed by cervical dislocation at day 15 following tumor inoculation. A cylindrical specimen with a diameter of 3 mm containing brain and tumor was explanted using augmented reality assistance (Schneider *et al.*, 2015) and fixed in 4 % phosphate-buffered formaldehyde using a straw. A straw was chosen as a thin container wall was required. The form-fitting container also reduced the likelihood of bubble formation. The total size of the specimen was $\sim 40\,\mathrm{mm}^3$.

2.2. Data acquisition

All *ex vivo* measurements were carried out at the beamline ID19 (European Synchrotron Radiation Facility (ESRF), Grenoble, France). For the illumination, a single-harmonic undulator (u17.6) was used with a mean photon energy of 19.6 keV. Hence, the bandwidth of the

radiation used for imaging is the native bandwidth of the harmonic of the source: around 10 %. The sample was first measured using XDGI, followed by a subsequent measurement using SDPR.

2.2.1. X-ray double-grating interferometry The interferometer consisted of a phase grating g_1 with a periodicity of 4.8 µm and a Si structure height of 23 µm, in order to induce a phase shift of π and an analyser grating g_2 with a periodicity of 2.4 µm and an Au structure height of 50 µm. The experiments were performed at the eleventh fractional Talbot order, resulting in an inter-grating distance of 465 mm. For the tomographic reconstruction, 1000 equiangular radiographs over 360° were recorded. For phase retrieval, the phase stepping technique (Weitkamp *et al.*, 2005), with four images over one period of the interference pattern at each projection angle was used. The detection system (FReLoN 2K, ESRF, Grenoble, France, lens-coupled to a scintillator screen (Douissard *et al.*, 2012)) had an effective pixel length of 5 µm and was placed about 3 cm downstream of grating g_2. Each image was acquired with an exposure time of 1 s resulting in a total acquisition time of around 3 h. For measurement, the specimen was located in a water tank with parallel polymethylmethacrylat plates around 10 cm upstream grating g_1, to increase sensitivity. Phase retrieval using Fourier analysis, and the reconstruction using a Hilbert transform in combination with a back-projection algorithm (Pfeiffer *et al.*, 2007*b*), was performed using in-house scripts in MATLAB® (2016a, The MathWorks, Inc., Natick, Massachusetts USA).

2.2.2. Single-distance phase retrieval For inline X-ray phase contrast using partially coherent illumination, no X-ray optical elements are required. Only a drift space between sample and detector is introduced, termed propagation distance. Due to propagation distance, recorded radiographs obtain both absorption and phase information. The phase information can be interpreted as Laplacian of the phase of the wavefront after transmitting the sample (Cloetens, 1999). Paganin *et al.* (2002) derived an algorithm for phase retrieval for single-component material based on the transportation of the intensity equation (TIE), if the object and the detector plane fulfill the near-field condition. Despite the assumption of a single-component material, the algorithm has proven itself to be robust also for multi-component materials, and soft tissue in particular (Lang *et al.*, 2014). SDPR measurements were performed at a sample-detector distance of 202 mm. Over 360°, 2000 equiangular projections were acquired. Radiographs were recorded using the FReLoN E2V (ESRF, Grenoble, France, lens-coupled to a scintillator screen (Douissard *et al.*, 2012)), with an effective pixel size of 1.87 µm. Exposure time per radiograph was 0.2 s resulting in a total acquisition time of around 27 minutes per height step. Due to the small effective pixel size, two height steps were necessary to image the whole sample, which were combined after reconstruction by translation registration using nearest neighbour interpolation. The phase retrieval itself was performed in ANKAphase (Weitkamp *et al.*, 2011) with a δ/β ratio of 1546, corresponding to the ratio for water for photons with an energy of 19.6 keV. The subsequently achieved phase projections were reconstructed using the standard filtered back-projection algorithm (Kak & Slaney, 1988) implemented in MATLAB® (2016a, The MathWorks, Inc., Natick, Massachusetts USA).

3. Results

The SDPR-slices contained dominant ring artefacts, as illustrated in Fig. 1. Their severity is also related to the low contrast provided by the specimen. The main reconstruction challenge was not only to remove

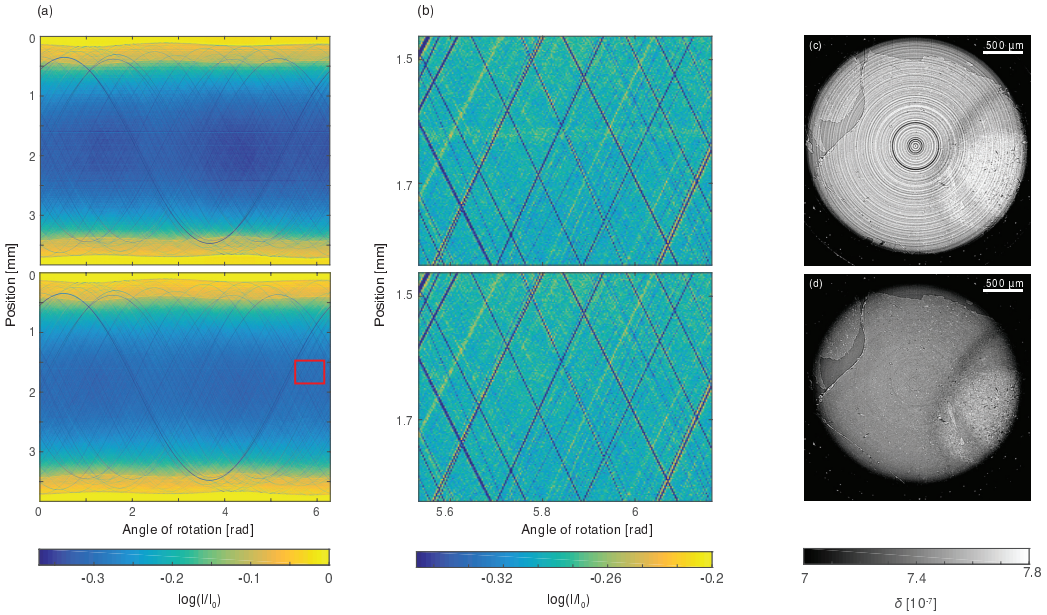

Figure 1
The ring artefact removal protocol used for the reconstruction of SDPR data: (a) The sinogram before phase retrieval, using standard weighting of the flatfields (left) and translation-registration of the flatfields prior to division (right), respectively. The region enclosed by the red rectangle is displayed in (b,top), while (b,bottom) shows the same zoom-in after subtracting a high-pass filtered mean projection. The tomographic slices reconstructed from the sinograms are displayed in (c) and (d), respectively, showing a characteristic slice of the specimen.

the ring artefacts, but also to maintain the radiographs' true information. To achieve this goal, we developed a reconstruction protocol for high-resolution tomography. We first improved false pixel mapping by using translation registration to map accurately the flatfields to the projections. The effect of flatfield registration is displayed in Fig. 1(a). The remaining artefacts were then removed by subtracting a high-frequency filtered averaged projection, see Fig. 1(b), taken for each projection over a range of 54°, i.e. 300 projections. A more detailed description of the ring-artefact compensation protocol is given by Thalmann *et al.* (2017*b*). Fig. 1(c) displays a phase-reconstructed slice, using the standard weighting of the flatfields. Fig. 1(d) shows the corresponding slice, using the developed ring artefact removal protocol.

Fig. 2 shows a cross-section through the centre of the tumor and indicates true cellular resolution with reasonable contrast provided by SDPR. Owing to the spatial resolution provided, individual cells are unequivocally identified across the whole specimen area, albeit more frequently inside the tumor, as expected. Blood vessels are also visualised, ranging from rela-

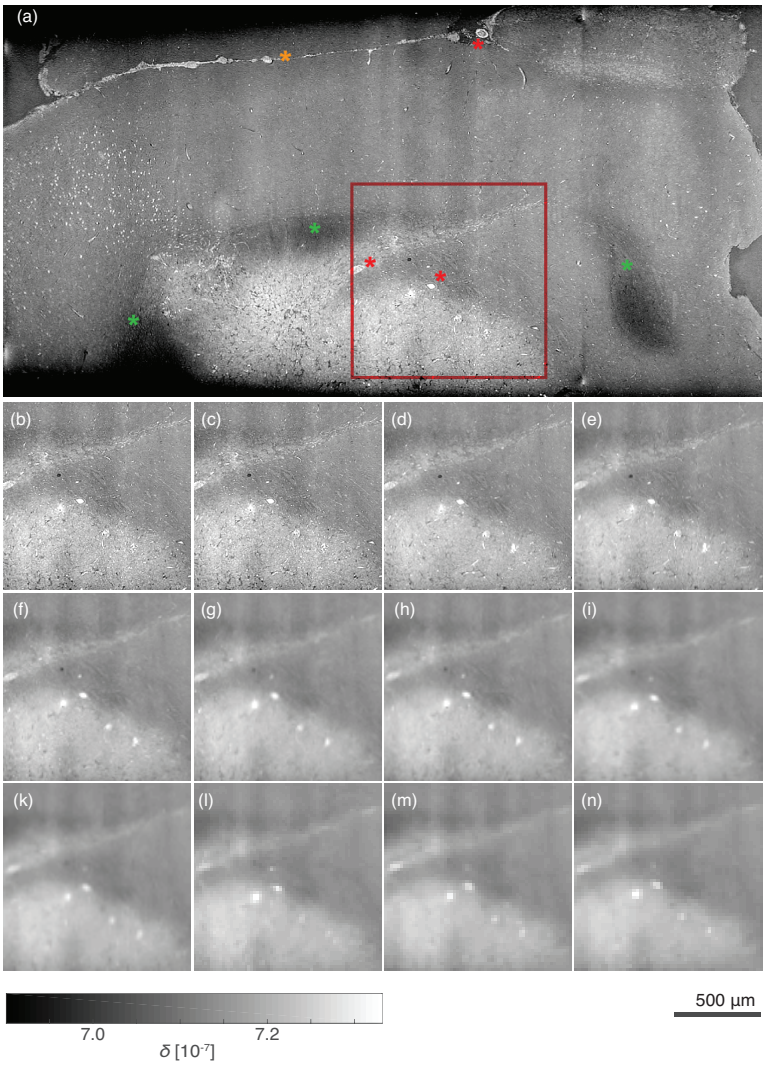

Figure 2
A cross-section of the mouse brain specimen with a tumor, visualised by means of SDPR. White matter tracts are indicated by green-coloured asterisks, major blood vessels are indicated by red-coloured asterisks and the location of the pia mater is shown by the orange-coloured asterisk. The region enclosed by the red square is displayed for binning factors of 1×1 (b), 2×2 (c), 3×3 (d), 4×4 (e), 5×5 (f), 6×6 (g), 7×7 (h), 8×8 (i), 9×9 (k), 10×10 (l), 11×11 (m) and 12×12 (n).

tively large examples (indicated by the red-coloured asterisks), to smaller capillaries. Nevertheless, to be able to distinguish the latter from cells, a three-dimensional approach is necessary. The contrast of the tomogram allows for distinguishing between the tumor, which shows an increased signal, and healthy brain tissue. Finally, the contrast provided by SDPR is also sufficient to identify clearly white matter tracts (green-coloured asterisks), as well as the pia mater (orange-coloured asterisk), from their surroundings. These findings were verified by histology. The top and bottom of the image in Fig. 2 are located at the specimen-container interface. High edge enhancement at the interface, caused by the strong local change in the refractive index, is not treated appropriately by the Paganin filter and becomes blurred, thereby causing a gradient at the specimen-container interface. For binning factors (BFs) up to six, an increase in contrast can even be identified by visual inspection.

This result is also supported by the findings in Fig. 3, showing the histograms for a selected ROI in the centre of the image, in order to minimise gradient effects induced by the container, including the three tissue types (white matter (WM), grey matter (GM), tumor (T)). The fitting parameters for the histograms are listed in Table 6, with the contrast-to-noise ratio (CNR) defined as $\mathrm{CNR}_i = |\mu_i - \mu_{Container}|/\sigma_{Container}$, where μ denotes the expectation value and σ the standard deviation of the corresponding Gaussian fit. The expectation values were almost constant for all BFs ($\mu_{GM} = 7.15 \pm 0.01$; $\mu_T = 7.20 \pm 0.05$; $\mu_{WM} = 7.09 \pm 0.03$). Spatial resolution, defined as the intersection between the normalised modulation transfer function (MTF) and its 10 % value (Thurner *et al.*, 2004; Müller *et al.*, 2002), was calculated using the sample-formalin interface.

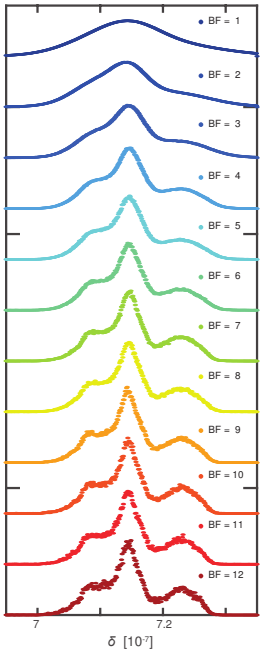

Figure 3
Illustration of the high increase in image contrast achieved by binning a selected ROI. The left peak corresponds to white matter (WM), the centre peak to grey matter (GM) and the right peak to the tumor (T). Gaussian fitting parameters are listed in Table 6.

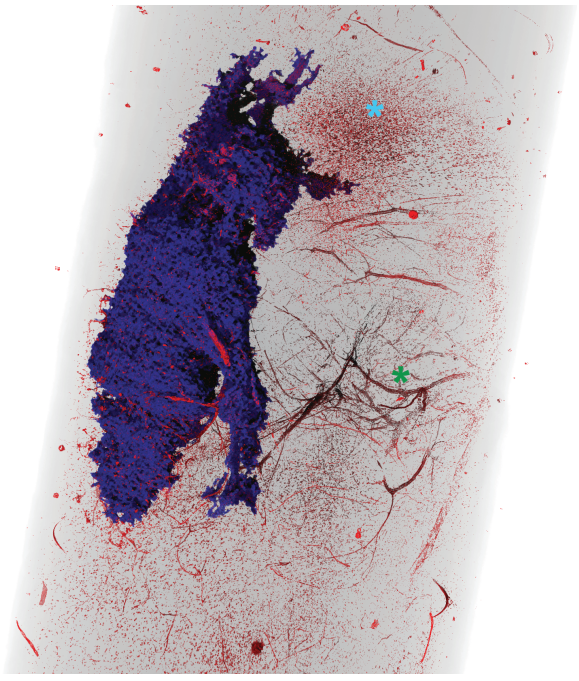

Figure 4
Observe the region (azure-coloured asterisk) close to the top of the tumor, presumably attributed to the inflammation reaction and bleeding around the needle insertion path. The larger vessels in the middle of the image (green-coloured asterisk) follow relatively aligned trajectories and indicate the existence of a white matter bundle at this location.

Table 6
Standard deviation (σ) of the Gaussian fits corresponding to white matter (WM), grey matter (GM) and the tumor (T), together with the contrast-to-noise ratio (CNR) for grey matter and the calculated spatial resolution (λ), for the datasets reconstructed with selected binning factors (BFs). Gr denotes the XDGI measurement.

BF	$\sigma_{GM}/10^9$	$\sigma_T/10^9$	$\sigma_{WM}/10^9$	CNR_{GM}	λ [µm]
1	4.22 ± 0.57	9.07 ± 0.24	5.51 ± 1.56	23.37 ± 0.06	2.17 ± 0.31
2	2.50 ± 0.04	6.10 ± 0.09	4.55 ± 0.07	27.16 ± 0.07	3.72 ± 0.19
3	2.18 ± 0.02	4.73 ± 0.05	3.50 ± 0.05	29.38 ± 0.09	5.60 ± 0.28
4	1.95 ± 0.02	3.58 ± 0.06	2.83 ± 0.06	32.28 ± 0.13	7.47 ± 0.37
5	1.89 ± 0.03	3.58 ± 0.07	2.77 ± 0.06	32.78 ± 0.15	9.34 ± 0.47
6	1.80 ± 0.03	3.30 ± 0.07	2.65 ± 0.07	34.70 ± 0.20	11.06 ± 0.56
7	1.68 ± 0.03	2.96 ± 0.07	2.58 ± 0.09	37.20 ± 0.26	12.88 ± 0.64
8	1.75 ± 0.03	3.00 ± 0.08	2.57 ± 0.09	37.52 ± 0.23	14.94 ± 0.75
9	1.74 ± 0.04	2.84 ± 0.09	2.42 ± 0.11	39.02 ± 0.28	16.81 ± 0.84
10	1.66 ± 0.04	2.78 ± 0.09	2.51 ± 0.12	39.23 ± 0.31	18.29 ± 0.91
11	1.72 ± 0.04	2.79 ± 0.10	2.49 ± 0.13	39.17 ± 0.30	20.06 ± 1.00
12	1.66 ± 0.05	2.74 ± 0.10	2.49 ± 0.14	39.74 ± 0.27	21.89 ± 1.09
Gr	0.86 ± 0.02	1.37 ± 0.03	0.62 ± 0.08	52.27 ± 0.91	21.55 ± 0.60

Table 6 shows that for a BF larger than or equal to two, the spatial resolution is close to its binned effective pixel size. However, an effective pixel size of 5.6 µm, i.e. reconstruction with a BF of three, was too large to resolve the smallest capillaries or the previously identified cells. In addition, the borders of the larger vessels, which remained identifiable, as well as the borders of the tumor itself and the finer white matter bundles, were also much less clear.

In order to achieve a crude segmentation of the tumor in the SDPR dataset, Otsu's method (Otsu, 1979) was applied to the histogram, after reconstruction with a BF of eight. The segmentation result, illustrated in Fig. 4, did provide an estimation of the tumor shape and location, but it was not satisfactory for the entire tumor volume. In particular, it completely failed close to the container, because of the induced gradient.

Fig. 5 better illustrates the differences between the non-binned XDGI dataset and the SDPR dataset using a BF of two. To allow for a comparison, the SDPR dataset was registered to its XDGI counterpart by means of rigid registration. Due to the limited amount of spatial resolution, XDGI was unable to resolve either the smallest vessels or the individual cells, as seen more prominently inside the tumor. The contrast between the tumor and the surrounding healthy tissue is superior for the XDGI dataset, as illustrated in Table 6. The most prominent difference is the fact that the electron density of the white matter bundles, indicated by the green-coloured asterisks in Fig. 5, appears to have changed between the two measurements. In essence, white matter appears to be less electron-dense than grey matter in the SDPR and more electron-dense in the XDGI dataset. In comparison, the site of injection shows less electron density than the grey matter in both measurements.

To increase the performance of tumor segmentation in the SDPR dataset, multi-modal information in the joint histogram, together with the XDGI dataset, was used. This approach is illustrated in detail in Fig. 6. The joint histogram of the SDPR and the XDGI datasets was Gaussian-blurred, and then a watershed algorithm was applied. The red path displayed in Fig. 6 (a) defines the boundary of the segmented tumor region. This segmentation result was then applied to the SDPR dataset, reconstructed with a BF of two. The improvement in segmentation can be seen in the three orthogonal cross-sections in Fig. 6 (b), where the tumor segmentation result using Otsu's method on the SDPR histogram alone (blue path) is compared to the improvement made by employing a watershed algorithm to the joint histogram of the SDPR and XDGI datasets (red path).

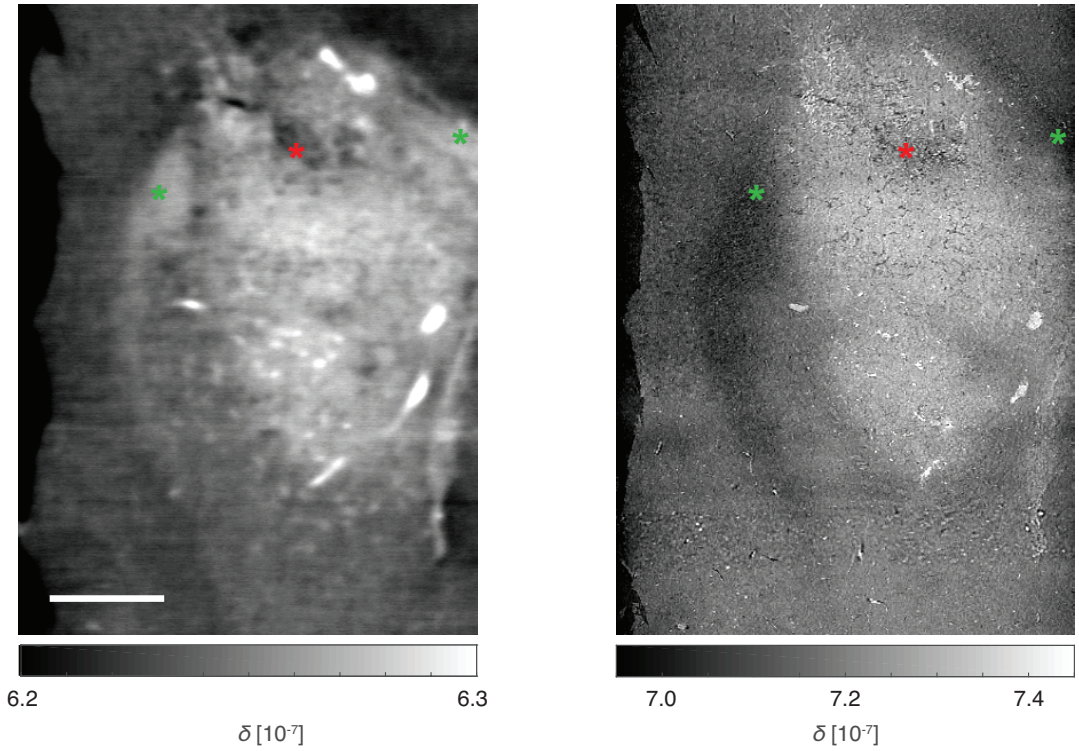

Figure 5
A cross-section of the XDGI (left) dataset compared to the SDPR dataset reconstructed with a BF of two (right), compared to XDGI (left). The green-coloured asterisks indicate white matter bundles, which appear to be less electron-dense than grey matter in the SDPR measurement, and more electron-dense than grey matter in the XDGI. The red-coloured asterisks indicate the site of injection, which, conversely to white matter, appears to be less electron-dense than grey matter in both the SDPR and the XDGI dataset. Bar length corresponds to 500 µm.

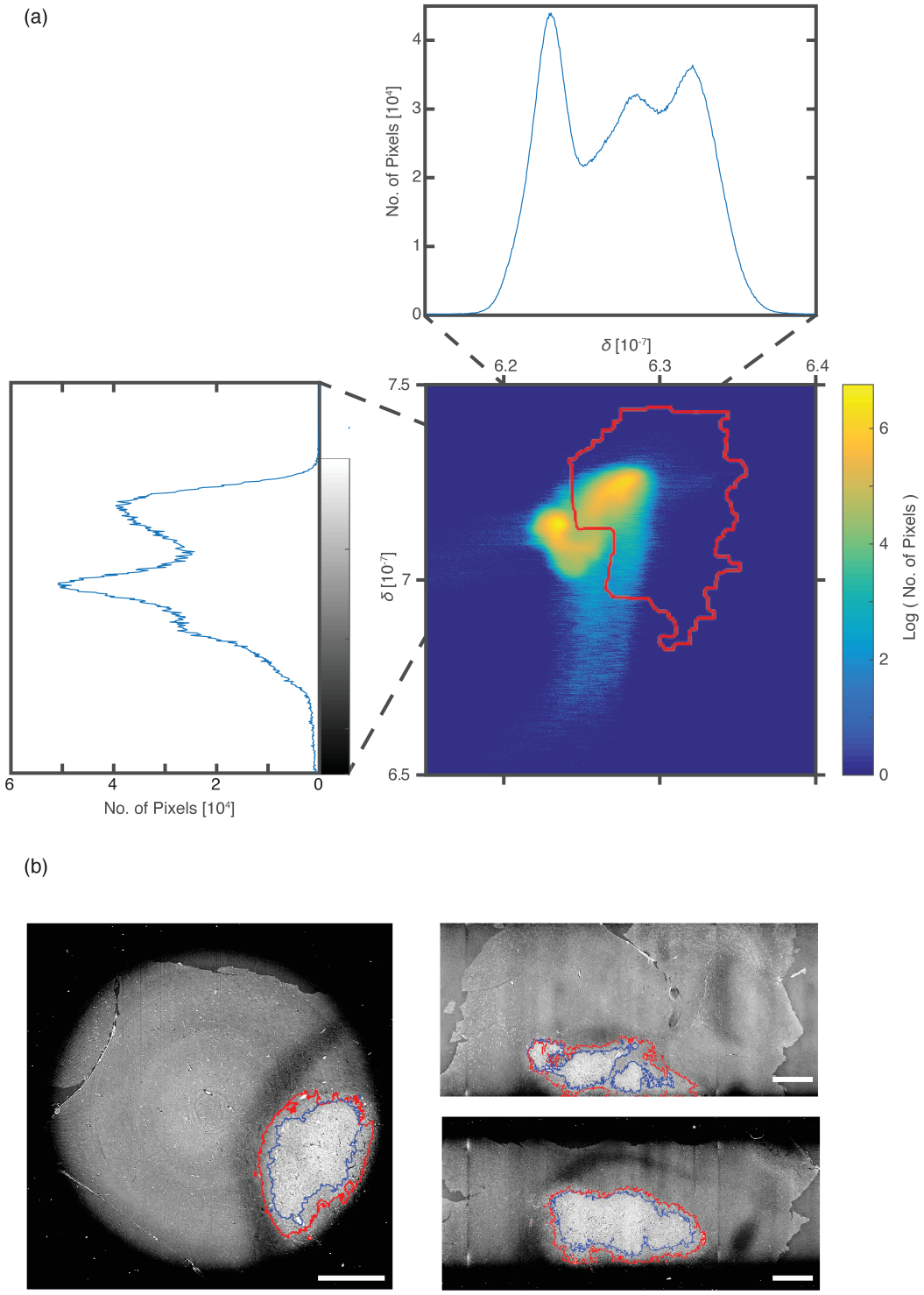

Figure 6
Figure (a) shows the joint histogram of the XDGI and SDPR datasets, reconstructed with a BF of eight of a selected ROI after rigid registration, and corresponding histograms. Figure (b) shows three cross-sections of the SDPR dataset, reconstructed with a BF of two. It illustrates the superiority of the segmentation based on joint histogram clustering using watershed transformation (red path) to the segmentation, using Otsu's method performed on the histogram of SDPR alone (blue path). Bar lengths correspond to 500 µm.

4. Discussion

In high-resolution, synchrotron radiation-based tomography, ring artefacts frequently originate either from particles and scratches on the scintillator or from improperly functioning pixel elements on the detector. However, beamline set-ups nowadays reach a high level of imaging sensitivity especially when they exploit the coherence of the impinging wavefront at the position of the experiment. Hence, such imaging setups are not only more sensitive to density variations within the specimen under study but also inhomogeneities introduced to the wavefront by the various X-ray optical elements required (such as beamline exit windows, attenuators). Tails in the point-spread function of the detector, potential source instabilities and distortions of the wavefront introduced by the sample itself therefore can lead to failure of simple flatfield approaches. Hence, the standard division of the recorded radiographs by its corresponding flatfield can be insufficient, due to improper pixel mapping, and thus result in prominent ring artefacts as displayed in Fig. 1(c). Instead of using standard ring artefact removal algorithms, which are normally applied to the sinogram or the slice itself, we corrected improper pixel mapping at an earlier stage of the reconstruction process, namely on the projections, using translation registration. All translations were in the subpixel range. Typically, the shift length was around 0.2 pixels. One drawback of a flatfield translation is that it blurs potential rings originating from scratches or dust particles on the scintillator, which are rigid with respect to the camera's sensor. The remaining line fragments can then easily be removed by subtracting a high-frequency filter averaged projection (Mirone *et al.*, 2014). A further advantage of this approach over standard techniques applied to the sinogram (Münch *et al.*, 2009) or the reconstruction slice (Sadi *et al.*, 2010) is that it does not treat each slice individually, and thus it maintains information between neighbouring slices.

After proper reconstruction, both techniques allowed for the visualisation of brain anatomy, including the cortex, the olfactory bulb, as well as several white matter bundles. The pia mater and capillaries were also visualised, although small capillaries, together with individual cells themselves, could only be visualised by means of SDPR. Most importantly for this study, both methods were able to detect the tumor compared to surrounding healthy tissue.

Many studies have already proven the superior contrast provided by XDGI, not only over standard absorption techniques (Pfeiffer *et al.*, 2007*a*), but also over in-line phase retrieval algorithms (Lang *et al.*, 2014), for the visualisation of soft tissues – as also validated by our study. However, in XDGI, the spatial resolution depends on the grating period of the analyser grating, and fabricating well-performing gratings with submicrometre periods is a challenging task. As a consequence, stagnation has been observed in the performance of the XDGI with respect to spatial resolution. Nevertheless, recent developments help avoid analyser grating by detecting the interference pattern directly with the camera (Zdora *et al.*, 2017). In this regard, it was also shown that the single-grating set-up can readily increase the spatial resolution (Thalmann *et al.*, 2017*a*) compared to the XDGI. In contrast, in in-line tomography, the spatial resolution can be increased easily by optical magnification. In our study, the smaller effective pixel size of SDPR allowed for the detection of several anatomical structures that could not be identified in XDGI. These include vessels smaller than 10 µm in diameter as well as individual cells, most prominently seen in the tumor itself. In order to make a meaningful comparison regarding the CNR, SDPR data were binned by a factor, such that the datasets being compared had a similar spatial resolution. Even in this case, XDGI still showed a higher CNR. Nevertheless, the CNR for SDPR in our study was found to be largely improved by an increased binning factor, especially for lower BF values, as highlighted in Table 6. Using a BF of eight even allowed for a rough segmentation of the tumor, using Otsu's method, followed by the selection of the largest connected component, which then can easily be re-sampled on the reconstructions with a smaller BF (see e.g. Fig. 4). Thus, despite the limited contrast provided, no sophisticated segmentation algorithm was necessary to get a rough approximation of the cancerous tissue, though it failed completely close to the sample holder, due to the induced gradient at the interface.

The joint histogram in Fig. 6 also leads to two significant observations. First, as already seen in other studies, there is a discrepancy in the δ values (Lang *et al.*, 2014; Huang *et al.*, 2015), which can be attributed to various factors (Lang *et al.*, 2014). In the SDPR techniques used herein, the condition of a constant δ/β-ratio may be violated to some extent. This was certainly the case for the container material, where the reconstructed decrements deviated the most ($\mu^{SDPR}_{Container} \approx 3.71$; $\mu^{DXGI}_{Container} \approx 5.55$). As far as the specimen itself is concerned, it is also likely that the selected δ/β was overestimated. While the main component of the specimen is certainly water, its lipid and protein content may explain the observed difference. Since XDGI does not depend on such assumptions it is well known to give quantitative results, the δ values provided by XDGI are therefore more reliable.

Second, the joint histogram in Fig. 6 also reveals inconsistent behaviour by the white matter signal between the XDGI and the SDPR measurement that followed. To investigate further the origin of this finding, the XDGI measurement was performed again, using the same setting. Prior to this repeat measurement, the specimen was embedded in histogel, to allow for easier storage and handling, without practically altering its composition. The three peaks for all the main sample components were then found to be in accordance between XDGI and SDPR, indicating that the observed difference for the white matter signal between the two XDGI measurements was caused by an event in between. A possible explanation for this behaviour is the well-documented sensitivity of myelin to several factors, among others, organic solvents and dehydration (Fernández-Morán & Finean, 1957; Finean, 1960). It is unclear, though, to what extent the initial XDGI measurement or subsequent SDPR ones contributed to this effect. This question needs to be addressed in a further study, to understand better the effect of synchrotron radiation on myelin-abundant samples.

The proposed method presents considerable advantages compared to existing microscopy modalities as far as the size of the investigated specimen is concerned and due to the fact that no contrast agent is needed. For instance, two-photon microscopy using fluorophores offers a penetration depth close to 1 mm, as seen, for example, in Morales *et al.* (2012). The administration of fluorescent probes prior to animal sacrifice is also associated with leakage from the fragile tumor vasculature into the tumor interstitium. A similar penetration depth of 1 mm is also offered by confocal microscopy, which has been used in recent years for *ex vivo* brain tumor detection (Forest *et al.*, 2015). Although usable results can be acquired without any fluorophore, the best results, as well as true cellular resolution, are only obtained with the use of staining, such as acridine orange. The need for a fluorescent probe or staining for imaging can be bypassed altogether by microscopy modalities such as multi-photon excitation of autofluorescence, but the penetration depth is even more limited, namely around a few hundred micrometres (Kantelhardt *et al.*, 2007). In any case, these microscopy modalities offer at best a penetration depth lower than 1 mm, which is inadequate for the non-destructive visualisation of murine brain tumors.

5. Conclusion

Synchrotron radiation-based phase tomography is a powerful technique to visualise tumors inside the mouse brain in a label-free manner. SDPR allows detecting single cells owing to the spatial resolution provided, here less than 3 µm for the non-binned reconstructed data. Binning the data by a factor of twelve, the spatial resolution becomes comparable to XDGI and the widths of the tissue peaks decreases by a factor of about three. This improvement is not enough to reach the CNR of XDGI. Combining the two complementary phase tomography approaches to a multi-modal method yields precise tumor localisation by means of joint-histogram clustering.

6. Acknowledgements

The authors thank Michele Bernasconi and Zsofia Kovacs from the University Children's Hospital in Zurich for their support during animal experiments and data analysis and Irene Zanette from the Diamond Light Source for her support during beamtime. The authors acknowledge the European Synchrotron Radiation Facility for the provision of beamtime at beamline ID19 under experiment number MD-860. The financial contribution of the Swiss National Science Foundation (Project Nos. 144535 and 147172) is gratefully acknowledged.

References

Als-Nielson, J. & McMorrow, D. (2011). *Elements of Modern X-ray Physics (2nd Edition)*. John Wiley & Sons Ltd.

Bonse, U. & Busch, F. (1996). *Progress in Biophysics & Molecular Biology*, **65**(1), 133–169.
URL: *http://www.sciencedirect.com/science/article/pii/S0079610796000119*

Cloetens, P. (1999). *Contribution to Phase Contrast Imaging, Reconstruction and Tomography with Hard Synchrotron Radiation*. Ph.D. thesis, Vrije Universiteit Brussel, Belgium.

Douissard, P. A., Cecilia, A., Rochet, X., Chapel, X., Martin, T., van de Kamp, T., Helfen, L., Baumbach, T., Luquot, L., Xiao, X., Meinhardt, J. & Rack, A. (2012). *J. Instrum.* **7**(09), P09016.

Fernández-Morán, H. & Finean, J. B. (1957). *J. Biophys. Biochem Cytol.* **3**(5), 725–748.

Finean, J. B. (1960). *J. Biophys. Biochem Cytol.* **8**(1), 13–29.

Forest, F., Cinotti, E., Yvorel, V., Habougit, C., Vassal, F., Nuti, C., Perrot, J.-L., Labeille, B. & Péoc'h, M. (2015). *J. Neurooncol.* **124**(2), 157–164.

Germann, M., Morel, A., Beckmann, F., Andronache, A., Jeanmonod, D. & Müller, B. (2008). *J. Neurosci. Methods*, **170**, 149–155.

Huang, S., Kou, B., Chi, Y., Xi, Y., Cao, Y., Cui, W., Hu, X., Shao, Z., Guo, H., Fu, Y., Xiao, T., Sun, J., Zhao, J., Wang, Y. & Wu, J. (2015). *Sci. Rep.* **5**, 9418.

Kak, A. C. & Slaney, M. (1988). *Principles of computerized tomographic imaging*. IEEE Press.

Kantelhardt, S. R., Leppert, J., Krajewski, J., Petkus, N., Reusche, E., Tronnier, V. M., Huttmann, G. & Giese, A. (2007). *Neuro-oncol.* **9**, 103–112.

Lang, S., Zanette, I., Dominietto, M., Langer, M., Rack, A., Schulz, G., Le Duc, G., David, C., Mohr, J., Pfeiffer, F., Müller, B. & Weitkamp, T. (2014). *J. Appl. Phys.* **116**(15), 154903.

Louis, D. N., Perry, A., Reifenberger, G., von Deimling, A., Figarella-Branger, D., Cavenee, W. K., Ohgaki, H., Wiestler, O. D., Kleihues, P. & Ellison, D. W. (2016). *Acta Neuropathol.* **131**(6), 803–820.

Mirone, A., Brun, E., Gouillart, E., Tafforeau, P. & Kieffer, J. (2014). *Nucl. Instrum. & Meth. in Phys. Res. B*, **324**, 41–48.

Momose, A. (2002). *J. Synchrotron Radiat.* **9**(3), 136–142.

Morales, A. R., Yanez, C. O., Zhang, Y., Wang, X., Biswas, S., Urakami, T., Komatsu, M. & Belfield, K. D. (2012). *Biomaterials*, **33**(33), 8477–8485.

Müller, B., Thurner, P., Beckmann, F., Weitkamp, T., Rau, C., Bernhardt, R., Karamuk, E., Eckert, L., Brandt, J., Buchloh, S., Wintermantel, E., Scharnweber, D. & Hartmut, W. (2002). *Proc. SPIE*.

Münch, B., Trtik, P., Marone, F. & Stampanoni, M. (2009). *Opt. Express*, **17**(10), 8567–8591.

Otsu, N. (1979). *IEEE Trans. Syst. Man Cybern.* **9**(1), 62–66.

Paganin, D., Mayo, S. C., Gureyev, T. E., Miller, P. R. & Wilkins, S. W. (2002). *J. Microsc.* **206**(1), 33–40.

Pfeiffer, F., Bunk, O., David, C., Bech, M., Duc, G. L., Bravin, A. & Cloetens, P. (2007*a*). *Phys. Med. Biol.* **52**(23), 6923–6930.

Pfeiffer, F., Bunk, O., Kottler, C. & David, C. (2007*b*). *Nucl. Instr. Meth. Phys. Res. A*, **580**(2), 925–928.

Sadi, F., Lee, S. Y. & Hasan, M. K. (2010). *Comput. Biol. Med.* **40**(1), 109–118.

Schneider, A., Thalmann, P., Pezold, S., Hieber, S. E. & Cattin, P. C. (2015). *Lecture Notes in Computer Science*, **9254**, 255–264.

Schulz, G., Morel, A., Imholz, M. S., Deyhle, H., Weitkamp, T., Zanette, I., Pfeiffer, F., David, C., Müller-Gerbl, M. & Müller, B. (2010*a*). *Proc. SPIE*, **7804**, 78040F.

Schulz, G., Weitkamp, T., Zanette, I., Pfeiffer, F., Beckmann, F., David, C., Rutishauser, S., Reznikova, E. & Müller, B. (2010*b*). *J. R. Soc. Interface*, **7**(53), 1665–1676.

Thalmann, P., Bikis, C., Hipp, A., Müller, B., Hieber, S. E. & Schulz, G. (2017*a*). *Appl. Phys. Lett.* **110**(6), 061103.

Thalmann, P., Bikis, C., Schulz, G., Paleo, P., Mirone, A., Rack, A. & Müller, B. (2017*b*). *Proc. SPIE*, **10391**, 1039114.

Thurner, P., Beckmann, F. & Müller, B. (2004). *Nucl. Instr. Meth. Phys. Res. B*, **225**(4), 599–603.

Weitkamp, T., Diaz, A., David, C., Pfeiffer, F., Stampanoni, M., Cloetens, P. & Ziegler, E. (2005). *Opt. Express*, **13**(16), 6296–6304.

Weitkamp, T., Haas, D., Wegrzynek, D. & Rack, A. (2011). *J. Synchrotron Radiat.* **18**(4), 617–629.

Zanette, I., Lang, S., Rack, A., Dominietto, M., Langer, M., Pfeiffer, F., Weitkamp, T. & Müller, B. (2013). *Appl. Phys. Lett.* **103**(24), 244105.

Zdora, M.-C., Vila-Comamala, J., Schulz, G., Khimchenko, A., Hipp, A., Cook, A. C., Dilg, D., David, C., Grünzweig, C., Rau, C., Thibault, P. & Zanette, I. (2017). *Biomed. Opt. Express*, **8**(2), 1257–1270.

2.3 Phase-contrast imaging and vessel analysis

In order to be able to investigate the structure of a vascular network in its entirety high-resolution three-dimensional imaging is required. SRμCT has proven itself to be a suitable imaging technique that allows visualizing the three-dimensional structure of the vascular network with a spatial resolution capable to resolve even the smallest capillaries. It has already been successfully applied in absoption-contrast mode for direct visualization of the vascular network using stainings and corrosion casts [6,7]. A prior investigation of murine colon carcinoma showed the potential of using synchrotron radiation-based in-line phase contrast tomography for the detection of the vascular network of a tumor in a label-free manner and thereby avoiding both leaking-related problems and tedious specimen preparation [31]. However, the study suffered from artifacts, such as for instance numerous non-connected vessel components [32]
In this study, we reinforce the potential of phase tomography based on SDPR for the analysis of vascular structures and tumor vasculature. The approach is benchmarked by investigating a mouse brain tumor at a true micrometer level. The segmentation of the vascular network revealed a preferential orientation of the vessels within the healthy tissue with the bigger ones being parallel one to the other. Contrarily, the vessels within the tumor showed a more chaotic behaviour. The quantitative analysis of the segmentation demonstrated that (i) the vessel density in the tumor was increased by a factor of two, (ii) the averaged radius of the tumor vessels is slightly larger, (iii) the longest vessels detected within the tumor were three times shorter, and (iv) tortuosity measures were also found to be increased for the case of the tumor. The technique enabled for the extraction of the vascular network including smallest capillaries in a labelfree manner and since the technique is non-destructive, it allows for subsequent histological analysis.

To be submitted (target Microvascular Research)

Comparing capillaries in healthy and cancerous tissues on the basis of hard X-ray phase tomography

Peter Thalmann[a], Christos Bikis[a], Marco D. Dominietto[a], Gabriel Schweighauser[b], Bert Müller[a], Simone E. Hieber[a]

[a] *Biomaterials Science Center, Department of Biomedical Engineering, University of Basel, Gewerbestrasse 14, 4123 Allschwil, Switzerland*
[b] *Institute of Pathology, Department of Neuropathology, University Hospital of Basel, 4031 Basel, Switzerland*

Abstract

The three-dimensional visualization of the vascular network by means of high-resolution computed tomography is usually achieved by using corrosion casts or the application of contrast agents. In cancerous tissue, vessel walls can be damaged and thus allow contrast agents to penetrate into the surrounding tissue. Synchrotron radiation-based micro computed tomography in phase-contrast mode provides sufficient to visualize and analyze the brain tissues in a label-free manner. In comparison to corrosion casts, phase tomography does not only reveal the vascular network, but also offers information on the entire specimen investigated, essential for investigating the relationship of tumors to their healthy surroundings. In the present quantitative phase tomography study, the capillary network of a mouse brain tumor, grown from injected murine glioma cells, during 15 days, together with surrounding healthy tissue was reconstructed, segmented, and quantitatively evaluated. The analysis of the vessel parameters points to the differences between the vasculature in healthy and cancerous tissues: (i) the vessel density in the tumor is a factor of two larger, (ii) the average vessel radius is slightly increased in the tumor, and (iii) tortuosity measures are larger in the tumor with respect to the surrounding tissue. Phase tomography, as a non-destructive technique, permits the subsequent histological analysis to validate the three-dimensional structural data via the two-dimensional optical micrographs.

Keywords: tumor, tortuosity, phase-contrast, synchrotron radiation, angiogenesis, vessel segmentation, bifurcation, vessel diameter, automatic characterization

---

Introduction

The concept of anti-angiogenesis as a therapeutic approach for tumor treatment is at least half a century old (Folkman, 1971). Last decade, inhibitors of the vascular endothelial growth factor (VEGF) have proven to be a useful adjuvant in tumor therapy (Jain et al., 2006). Nevertheless, their effectiveness is among others, reduced by the fact that in a tumor, there exist at least six different vessel types, four of which are absent in healthy tissues (Nagy et al., 2009). With VEGF, the most promising anti-angiogenic target at the time presumably only playing a major role for two of the tumor vessel categories, research is ongoing for more therapeutic targets to yield a synergistic effect. In addition to a better mechanistic understanding of angiogenesis at a molecular level, improved micro-anatomical knowledge of the tumor vasculature is necessary, given the fact that the percentage of existing vessels of different types can be used as a prognostic factor (Akslen et al., 2011). Furthermore, experimentally determined parameters are required for the validation of tumor growth simulations, allowing to examine the influence of initial conditions and local environment (Cai et al., 2016).

Towards this goal, visualization of the vessel tree down to the smallest capillaries is essential, due to the intrinsic tumor heterogeneity that arises at a genetic level and is passed down to molecular, anatomical and microvascular levels (Burrell et al., 2013; Meacham and Morrison, 2013). Heterogeneity is also influenced by the local tumor micro-environment, leading to an apparently chaotic growth of tumor structures, including the vessels, which are non-organized, tortuous and leaky, with a tendency to haemorrhage. The macroscopic tumor structure therefore consists of multiple domains with characteristic molecular signatures, cellular compositions, and consequently specific physiological behaviour. This

situation is well described for several types of cancer, including glioblastoma (Friedmann-Morvinski, 2014) and breast cancer (Beca and Polyak, 2016).

A suitable imaging method should thus visualize the tumor in its entirety. Additionally, contrast agents are to be avoided due to the risk of leaking. Finally, given that the tumor vascular network is mainly composed of capillaries and small vessels, with a diameter at the order of 10 µm, true micrometer resolution is required for the visualization of the entire vessel tree, a task that cannot by achieved by current *in-vivo* methods such as magnetic resonance imaging (MRI) or conventional computed tomography (CT).

Given the aforementioned requirements, synchrotron radiation-based micro computed tomography (SRµCT) is a suitable imaging technique that allows to visualize a complete three-dimensional (3D) structure of the vascular network with a spatial resolution capable to resolve even the smallest capillaries. SRµCT has already been successfully applied for direct visualization of the vascular network using stainings and corrosion casts (Plouraboue et al., 2004; Müller et al., 2006).

Without the use of contrast agents, SRµCT in absorption contrast mode does not provide sufficient contrast for the visualization of non-stained brain tissues (Schulz et al., 2010). However, for photon energies $\geq 10\,\mathrm{keV}$, and far from any absorption edges, for tissues with a low atomic number the total phase-scattering cross-section can be three orders of magnitude greater than the total absorption cross-section (Bonse and Busch, 1996; Momose, 2002; Als-Nielson and McMorrow, 2011) and is therefore preferential for the investigation of brain tissue. As grating interferometry has not yet provided results with the necessary spatial resolution for centimetre-sized specimens (Thalmann et al., 2017a), in-line phase tomography is preferred here.

Due to propagation distance, the recorded radiographs contain both phase and absorption information, where the phase information can be interpreted as the Laplacian of the phase of the wavefront after transversing the sample (Cloetens, 1999). In 2002, Paganin et al. (2002) derived an algorithm for phase retrieval of a single-component material based on the transport of the inten-

sity equation (TIE) (Teague, 1983), under the assumption that he object and the detector plane fulfil the near-field condition. Despite the fact that the assumption of a single-component material is violated by investigating biomedical specimens, the algorithm has proven itself to be also robust for the investigation of multi-component materials, and soft tissue in particular (Lang et al., 2014). For energies far from absorption edges the reconstructed refractive index decrement $\delta(x, y, z)$ is proportional to the local electron density.

A prior investigation of murine colon carcinoma showed the potential of using SRμCT in phase contrast mode, allowing a label-free imaging of tumorous tissues and therefore avoiding contrast-agents. The associated leaking problems are eliminated and the systematic errors introduced by tedious preparation are reduced (Lang et al., 2012). However, the study itself suffered from artifacts, including numerous non-connected vessel components (Müller et al., 2012). Recently, SRμCT with a voxel length of 8 μm has been combined with MRI with a voxel length of 40 μm in a multimodal approach, but the spatial resolution was still not capable of uncovering the smallest capillaries or giving a deep analysis of the tumor heterogeneity (Cebulla et al., 2014).

In this study we reinforce the potential of SRμCT in phase-contrast mode for the analysis of vascular structures and tumor vasculature in particular. We benchmark this approach by investigating a mouse brain tumor at a true micrometer level. We show that the technique enables for the extraction of the vascular network including the smallest capillaries and thus allows for advanced tortuosity analysis for the characterization of the vasculature.

Materials and Methods

Specimen preparation

A nude mouse (CD-1-Foxn1nu, Charles River Laboratories, France) eight weeks of age, weighting 24 g was used for the experiment. The injection of murine glioma cells (GL261 cells) into the right frontal lobe was performed using a stereoactic frame for head fixation. The animal also received analgesic (Flu-

nixin, 2 µL/g) and antibiotic treatment (Borgal, MSD Animal Health GmbH, Luzern, Switzerland) for the week after surgery.

In-vivo magnetic resonance experiments were performed using a PharmaScan 47/16 MRI system (Bruker BioSpin, Ettlingen, Germany) equipped with a 4.7 T magnet with 16 cm bore diameter and a cryogenic quadrature RF surface transmit/receive coil (Bruker BioSpin Ettlingen, Germany). During *in-vivo* experiments, the mouse was anaesthetized using isofluorane (1.5 % to 2 %), delivered via face mask using a mixture of air and oxygen in a ratio 4:1 and placed on a customized mouse support equipped with a stereotactic system for animal fixation. A cannula for the administration of contrast agent was inserted into the right tail vein.

The animal was monitored to daily check health conditions following a predefined scoring protocol. All the experiments were performed in strict adherence to the Swiss law for animal protection and were approved by the local authorities (license ZH 168/2010).

At day 15 after tumor inoculation, the mouse was euthanized by cervical dislocation. The brain was directly extracted and fixed in 4 % phosphate-buffered formaldehyde. Subsequently, it was scanned using the PharmaScan 47/16 MRI system with a resolution of 0.1 mm x 0.1 mm x 0.7 mm to localize the tumor position. A 3D navigation system based on augmented reality was developed and used for high precision sample extraction (Schneider et al., 2015). A cylindrical brain tissue sample including as much cancerous tissue as possible, together with healthy regions, was extracted using a sterile hypodermic needle with an outer diameter of 3 mm and was 4 % phosphate-buffered formaldehyde.

Data acquisiton

In-line single-distance phase-contrast based (SDPR) SRµCT was carried out at the beamline ID19 (ESRF, Grenoble, France). The measurements were performed at a sample-detector distance of 202 mm. Over the range of 360°, 2000 equiangular radiographs were acquired using the FReLoN E2V (ESRF, Grenoble, France, lens-coupled to a scintillator screen), at an effective pixel size of

1.87 µm. The exposure time per radiograph of 0.2 s resulted in a total acquisition time of around 27 minutes per height step. Because of the chosen effective pixel size, two height steps were necessary to image the entire sample. They were combined by translation registration using nearest neighbour interpolation. The phase retrieval itself was performed in ANKAphase (Weitkamp et al., 2011) with a δ/β-ratio of 1546 corresponding to the ratio of water for photons with an energy of 19.6 keV.

The sensitivity which is required of the employed beamline setups to perform such measurements, also turns the imaging system more susceptible to inhomogeneities introduced on the impinging wave fronts, that can result in severe ring artifacts. For artifact removal in the reconstruction process we followed the ring artifact removal proposed by Thalmann et al. (2017c), which partially removes potential artifact sources already in the projections by using translation-registration of the flat-fields and therefore maintains more of the true information of the projection. The translation registration itself was performed using ITK (2017). The subsequent reconstruction of the corrected phase projections was performed using the standard filtered back-projection algorithm (Kak and Slaney, 1988) implemented in MATLAB®(2016a, The MathWorks, Inc., Natick, Massachusetts USA).

The specimen was also measured by X-ray double grating interferometry. The phase grating g_1 had a periodicity of 4.8 µm and a Si structure height of 23 µm and thus induced a phase shift of π. The analyser grating g_2 had a periodicity of 2.4 µm and an Au structure height of 50 µm. The experiments were performed at an inter-grating distance of 465 mm, corresponding to the eleventh fractional Talbot order. Over the range of 360°, 1000 equiangular radiographs were recorded. For phase retrieval, the phase stepping technique (Weitkamp et al., 2005), with four images over one period of the interference pattern at each projection angle was used. The detection system (FReLoN 2K, ESRF, Grenoble, France, lens-coupled to a scintillator screen (Douissard et al., 2012) operated with an effective pixel length of 5 µm and was placed around 3 cm downstream of grating g_2. The exposure time per image was 1 s resulting in a total acquisition

time of around 3 h. For measurement, the specimen was placed around 10 cm upstream grating g_1 in a tank with parallel polymethylmethacrylat plates filled with distilled water to increase sensitivity. Phase retrieval using Fourier analysis, and subsequent reconstruction using a Hilbert transform in combination with a back-projection algorithm (Pfeiffer et al., 2007) was performed using in-house scripts in MATLAB® (2016a, The MathWorks, Inc., Natick, Massachusetts USA).

After the tomography measurements, the specimen was dehydrated in ascending ethanol solutions, transferred to xylenes and embedded in a paraffin/plastic polymer mixture (Surgipath Paraplast, Leica Biosystems, Switzerland), according to standard pathology protocol. By means of a microtome, sections 4 µm thick were produced, mounted on glass slides and stained with haemtoxylin and eosin (H&E). The obtained slices were scanned using a microscope slide scanner (3D Histech Panoramic MIDI, Sysmex Suisse AG) with an effective pixel size of 243 nm.

Image segmentation and analysis

Although phase tomography provides superior contrast compared to the absorption modality, vessel segmentation by simple thresholding is not feasible. Thus, more sophisticated segmentation tools are required.

Vessel segmentation and analysis was performed within the framework provided by (TubeTK, 2017). In order to call the final segmentation algorithm which not only segments but also directly labels the vessels, a vessel probability map has to be calculated.

In 1998, (Frangi et al., 1998) proposed a multiscale vessel enhancement filtering method based on the eigenvalues $\lambda = (\lambda_1, \lambda_2, \lambda_3)$ of the 3D Hessian matrix (Sato et al., 1998), where the return function is a probability of whether a voxel belongs to a vessel. Frangi et al. (1998) proposed the following vesselness

function of the scale s

$$V_0(s) = \begin{cases} 0 & \text{if } \lambda_2 > 0 \vee \lambda_3 > 0 \\ \left(1 - \exp\left(\frac{R_A^2}{-2\alpha}\right)\right) \exp\left(\frac{R_B^2}{-2\beta}\right) \left(1 - \exp\left(\frac{S^2}{-2c}\right)\right) & \text{otherwise} \end{cases}$$

where the ratio $R_A = |\lambda_2|/|\lambda_3|$ allows to distinguish between plate-like and line-like features. The ratio $R_B = |\lambda_1|/\sqrt{|\lambda_2\lambda_3|}$ accounts for deviation from blob-like structure, however is not capable to distinguish between line- and plate-like features. S denotes the Frobenius matrix norm of the 3D Hessian matrix, i.e. $S = \|\mathcal{H}\|_F = \sqrt{\sum_{j \leq D} \lambda_j^2}$ for the second order structures. α, β and c are thresholds controlling the sensitivity of the line filter to the measures R_A, R_B and S. The sign of the eigenvalues λ_2 and λ_3 reflects whether dark vessels reside in a bright background or vice versa. Finally, the vesselness measure is the maximum value of the vesselness function within a given range $s_{min} \leq s \leq s_{max}$.

For the preliminary segmentation, the Gaussian smoothing 3D multiscale Hessian-based filter from the open-source library (ITK, 2017) was used. Some compromises to the scale range were necessary and the scale was thus chosen from 1 to 15 voxels (∼1.8 µm to 25 µm). The parameter $\alpha = 0.5$, $\beta = 0.5$ were selected to extract the existing tubular structures and the parameter $c = 5$ accounted for the noise. The histogram of the resulting vesselness distribution showed an exponential decay. The cut-off vesselness for the data binarization was chosen approximately 0.7 % of the maximal vesselness for the healthy tissue. Since the chosen threshold was rather small, other structures were detected as well, e.g., single cells. However, exploiting the fact that vessels, due to their connectivity, contain a lot of voxels the binarized image was labelled by a connected component filter and every structure which was smaller than 1000 voxels was removed from the segmentation.

Within the tumor the segmentation was more tedious, as the recorded phase signal was increased in comparison to the healthy tissue, due to the numerous cells within the cancerous tissue. In order to be able to segment the vessels from the surrounding tissue the cut-off vesselness for the tumor had to be increased to around 1 % of the maximal vesselnes. Furthermore, all voxels within the

vesselness image, which yielded a refractive decrement $\delta \leq 7.5$ were set to zero before removing all objects smaller than 1000 voxels.

The correctness of the segmentation was verified by visual inspection, more precisely, by overlaying the resulting segmentation over the tomogram using Slicer (Kikinis et al., 2014). The binary image was converted to a nonzero data set for the final analysis performed in (TubeTK, 2017) by adding Gaussian noise.

For the analysis, a region of interest of approximately $4\,\mathrm{mm}^3$ was selected. Tumor localization was performed by joint-histogram clustering of the two acquired phase tomograms (Thalmann et al., 2017b).

Results

Interpretation of phase tomography data using histology

Fig. 1 shows a cross-section through the tumor investigated (left), along with a related histological slice (right), at a plane that is titled approximately by 25° with respect to the sagittal. The olfactory bulb, identified at the bottom left of the section, can be used for relative orientation. The contrast in the reconstruction is sufficient to distinguish between cancerous and healthy tissues. Along the tumor borders, several white matter bundles are visible. The tomography data, does not only allow distinguishing between gray and white matter, but also to identify individual cells and capillaries, with the results of SDPR being verified by histology. The tumor is preferentially expanded into the gray, rather than the white matter. The increased µCT signal within the cell-dense tumor originates from the fact, that cell nuclei are high-absorbing in µCT, appearing as very bright spots for a pixel size around 1 µm (Hieber et al., 2016). Nevertheless, it is often challenging to distinguish between a cell and a capillary cross-section in the two-dimensional representation, even within the healthy tissue, hence using the three-dimensional information is necessary. Comparison of the µCT scan of the formalin-fixed specimen to the histological section also reveals a size reduction at the order of 35 % induced by the dehydration and paraffin-embedding.

The amount of shrinkage matches the expectations presented in the literature Gundersen et al. (2013).

Differentiation between tumor and healthy brain tissue

Fig. 2 shows the segmentation of the vascular network obtained by means of a 3D multiscale Hessian-based filter. Within the healthy region, vessels follow a preferential orientation, with the bigger ones being parallel one to the other. Contrarily, a hierarchy of vessels is less visible in the tumor and vascularization is shown more interconnected and chaotic in nature.

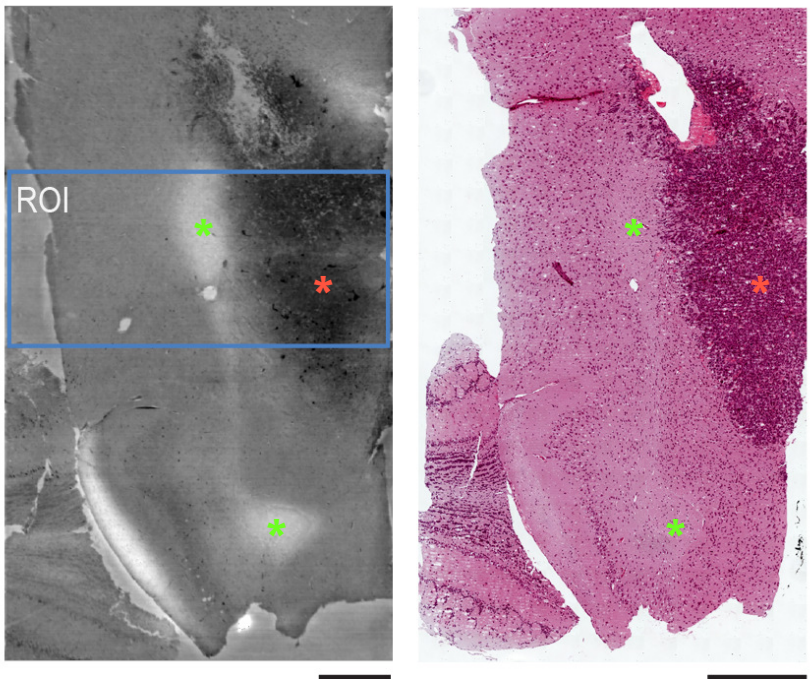

Figure 1: Side-to-side view of a µCT slice (left) and a corresponding H&E histological section (right). Several white matter tracts (green-colored asterisks) can be seen around the borders of the cell-dense tumor (red-colored-asterisk). The region of interest (ROI) used for the analysis is indicated by the blue rectangle. The scale bar in both images corresponds to 500 µm and reveals a 35 % shrinkage of the specimen that occurred between the formalin-fixed (left) and the paraffin-embedded (right) state.

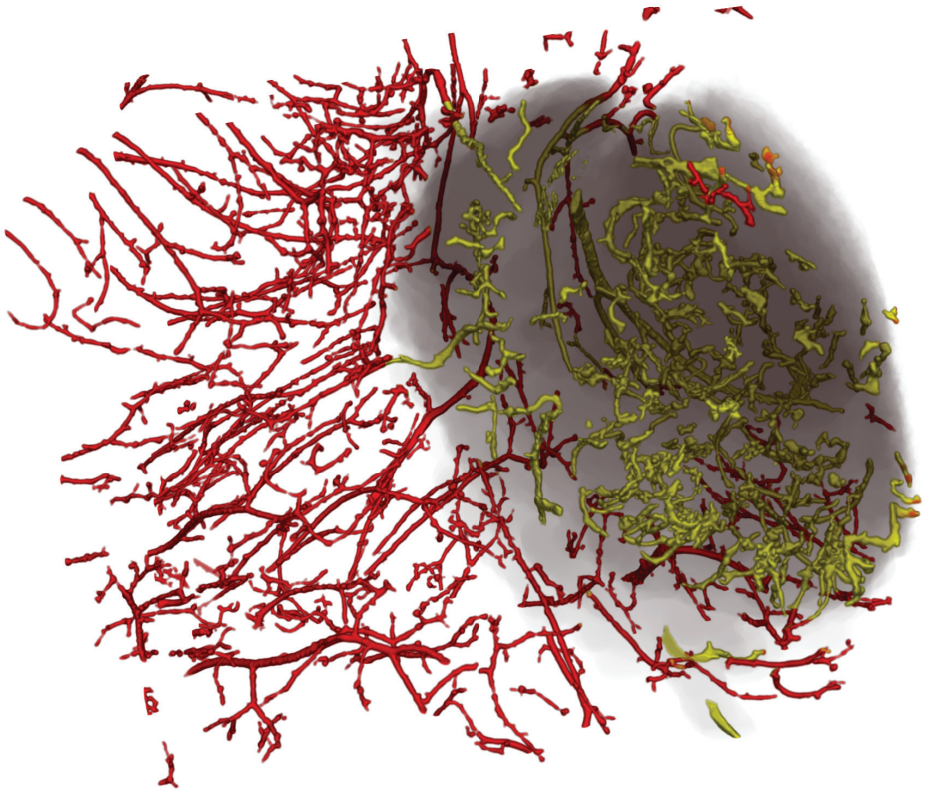

Figure 2: This figure illustrates the performance of the 3D multiscale Hessian-based filter for vessel extraction, applied in a box of dimensions 1.4 mm × 2.0 mm × 1.3 mm Observe the ordered vessels in the healthy region, which show a preferential orientation, while the vessel tree within the tumor appears chaotic.

Parameters of the vessel system

After segmentation, a quantitative description of the vasculature was performed and the folllowing distance and tortuosity metrics were investigated: Number of vessels per volume (T/V), vascular volume fraction (Vo/V), averaged radius (AR), path length metric (PLM), sum of angles metric (SOAM), distance metric (DM), inflection count metric (ICM), $\tau 4$ metric (T4M) defined as the sum of the norm of the curvature vector divided by the path length, and the percentile 95 metric (P95M) defined as the value for which 95 % points have a smaller curvature vector norm (TubeTK, 2017; Bullitt et al., 2005). The results

listed in Tables 1 and 2 were achieved by taking the median of the calculated measures for the individual vessels. Structures with an averaged radius $\leq 1\,\mu m$ where excluded from the analysis, as they could not correspond to vessels.

Vessel density

The vessel density was increased within the tumor in comparison to the healthy brain, i.e., the density of detected vessels was increased by 63 % and the density of vessel voxels by 43 %. This is also in accordance with the visualization in Fig. 2, where the vessel density in the tumor appears to be more dense.

Vessel radius

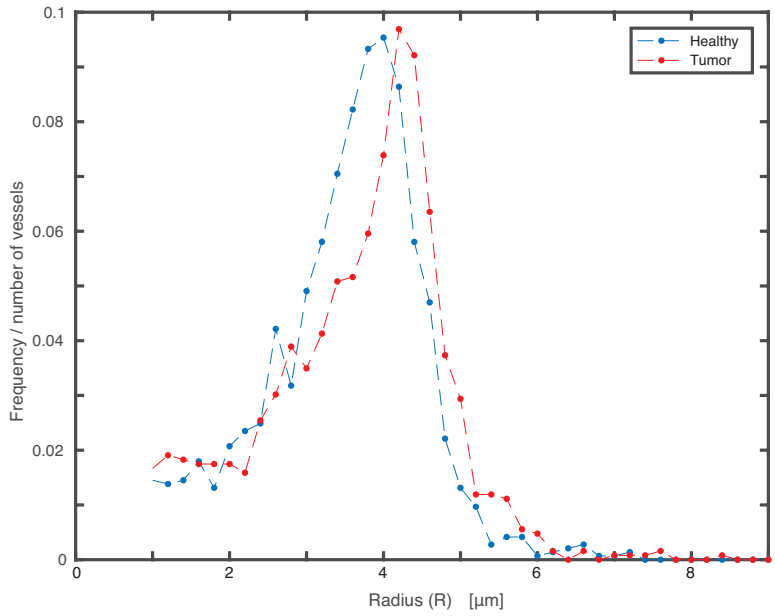

Figure 3: Histogram of the calculated average radius for vessels within the healthy (blue) and cancerous tissues (red). The histogram is normalized by the total number of detected vessels for each region. The average radius was slightly larger in the tumor with respect to the surrounding healthy tissue.

The analysis of the radius shows an increase of the averaged vessel radius within the cancerous tissue by 5 %. In addition, for both regions investigated

there are only a few vessels with a radius larger than 6 µm, as illustrated in Fig. 3.

Vessel length

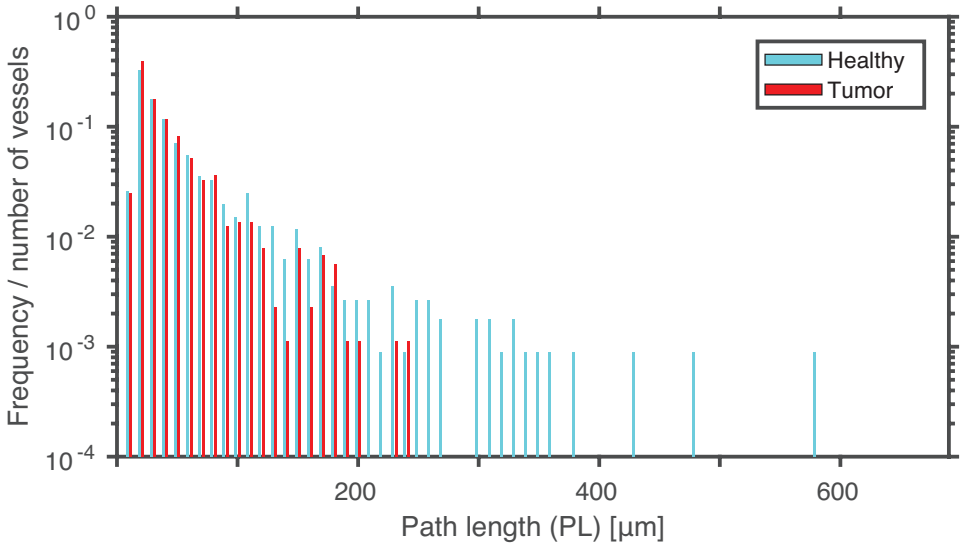

Figure 4: Histogram of the vessel length within the healthy (blue) and cancerous tissues (red). The histogram is normalized by the total number of detected vessels for each region. The vessels within the tumor are hardly longer than 200 µm.

The analysis showed that average vessel length tends to be slightly shorter within the tumor compared to the healthy brain, see Table 1. Furthermore, the histogram displayed in Fig. 4 shows that within the tumor there were practically no vessels longer than 200 µm.

Vessel tortuosity

All tortuosity metrics were increased for the tumor in comparison to the healthy brain. The most significant difference was observed for the ICM, which was almost doubled within the tumor. Fig. 5 shows the dependence of T4M on the vessel path length, where the absence of longer vessels results in a cut-off length of around 200 µm. The figure indicates, that longer vessels appear to

Table 1: Median values of the calculated vessel density and length parameters for healthy tissue and tumor. The calculated parameters are: Number of vessels per volume (T/V), number of vessel voxels per volume (Vo/V), averaged radius (AR), and path length metric (mPLM).

	T/V $[10^{-6}]$	Vo/V $[10^{-4}]$	AR [µm]	PLM [µm]
Healthy	4.42	3.74	3.69	27.69
Tumor	7.22	5.32	3.82	24.07

Table 2: Median values of the calculated tortuosity parameters for healthy tissue and tumor. The calculated parameters are: Sum of angles metric (SOAM), distance metric (DM), inflection count metric (ICM), $\tau 4$ metric (T4M), and percentile 95 metric (P95M).

	SOAM [rad/µm]	DM [-]	ICM [-]	T4M [μm^{-2}]	P95M [μm^{-1}]
Healthy	0.09	1.05	3.34	4.26	0.49
Tumor	0.12	1.10	6.31	4.61	0.66

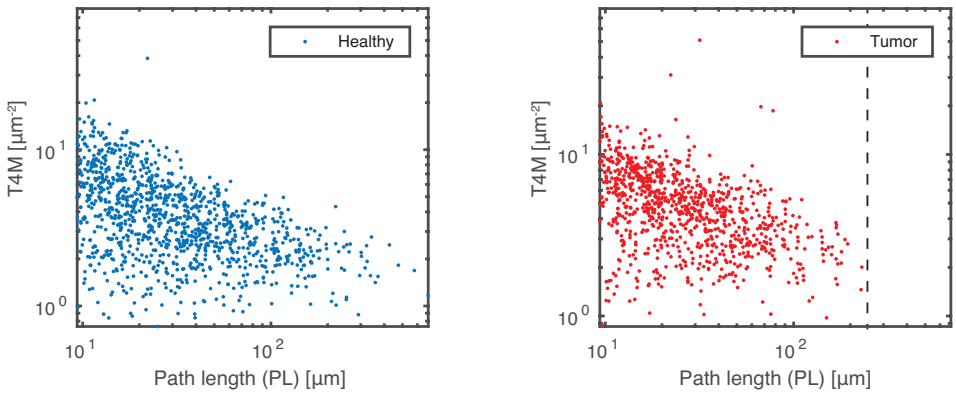

Figure 5: T4M metric plotted against the path length for the healthy (blue) and cancerous tissue (red). Observe the cut-off around 200 µm in the case of the tumor.

have a reduced mean local curvature.

Discussion

We have successfully applied SRμCT for the visualization and characterization of a tumor vessel tree, along with the vessels of the surrounding healthy tissue. Our method requires practically no additional processing after standard formalin fixation and can thus take place immediately after excision. We have also demonstrated that it is perfectly compatible with standard histology that can be performed afterwards, but also brings the added advantage of avoiding strong tissue shrinkage and deformations due to dehydration and paraffin embedding. Artefacts induced by sectioning and staining, that are often prevalent in histological slices, are also avoided. In-line phase tomography also eliminates the usage of contrast agents or the need for approaches such as corrosion casts. Such a label-free approach does not suffer from artefacts due to contrast agent leakage, that are a common occurrence for damaged tumor vessel walls when investigated by standard absorption μCT. Compared to corrosion casts that only allow for the visualization of the vascular network, phase tomography offers a far superior insight, by providing information on the entire specimen investigated. For instance, anatomical localization is much more precise, cell density can be quantified and other findings such as haemorrhage or oedema can be determined. Among the phase tomography modalities SDPR was chosen as, after ring artifact removal, it provided tomograms with sufficient contrast and adequate spatial resolution for the extraction of the vessel tree down to the smallest capillaries.

Intensity thresholding was insufficient for the segmentation of the vascular network, especially inside the cell-dense tumor. Therefore, a 3D multiscale Hessian approach was selected owing to its proven effectiveness in vessel segmentation (Frangi et al., 1998; Lang et al., 2012; Preim and Botha, 2013).

The largest vessels were neglected for further analysis, because they were partially filled with remaining blood making the segmentation challenging. In addition, these large vessels were not in the focus of the study. Even without contrast agent at all, connectivity of the segmented vascular network was

present, see Fig. 2. However, for the smallest capillaries image contrast was weak. The vessel wall cells as well as the haemoglobin content are presumably the two main sources of contrast. Thus, thin walls and little amount of blood might be the underlying reason for the occurrence of weak contrast for the smallest capillaries. These vessel segments were removed from the analysis, when all objects smaller than 1000 voxels were removed, which was necessary to eliminate individual cells. Contrarily, in this manner, the resulting connectivity of the vessels could be readily improved. The exclusion results in the overestimation of the averaged radius and an underestimation of the vessel density. Indirectly, it also affects the other averaged values calculated. The non detected vessels are expected also to have a short path length. In order to verify the meaningfulness of our data we plotted the results against the path length, see supplementary material. There are no sudden changes within the given distributions and only a little number of outliers. Within the tumor the situation is even more challenging. Due to the higher cell density, the vessel contrast within the tumor was weaker and, therefore the segmentation was impeded within this region and the percentage of detected capillaries was reduced, see Fig. 1.

After segmentation, the 3D vectorization provided by the framework of TubeTK (2017) was performed to allow for the extraction of the quantitative parameters. Vectorization was less successful for the larger vessels within the tumor. These vessels showed irregular cross-sections, combined with non-uniform phase signal within their lumen. As a result, some of them where erroneously detected as multiple vessels. This error results not only in an underestimation of the averaged radius and an overestimation of T/V, but since these tubes are artificially generated, they affected all calculated averages. It is assumed, that they did not affect the analysis significantly due to their limited number. In addition, several vessels showed a radius smaller than 1 µm. These vessels were considered artificial and excluded from the analysis. The lower contrast for small vessels did also generate discontinuities in the vessels causing the algorithm to label the separated vessel segments differently. Thus, for some vessels chord- and path length gets underestimated, and thereby also affects the related

tortuosity measures. All the above mentioned occurrences are presumed to be limited and therefore the comparison of the calculated parameters derived for the tumor with respect to the surrounding tissue is expected to meaningful.

The averaged vessel radius was slightly increased within the tumor, in accordance with the literature (Jain et al., 2006). The vessel number density (T/V), as well as the number of vessel voxels (Vo/V) were also increased within the tumor by a factor of about 1.5 and thus indicate increased microvasucularity within the cancerous tissue.

All tortuosity measures were also found to be larger for the case of the tumor. The findings displayed in Fig. 5, which shows a reduced mean local curvature for longer vessels can be directly observed in Fig. 2, where within the healthy brain the larger vessels appear parallel to each other and show a preferential orientation. Due to the small distance between nearest bifurcation points there should be no space for high-frequency wiggles to develop. Such wiggles would drastically increase DM, which was not observed, and thus, underlying the above statement. Contrarily, the increased ICM (Bullitt et al., 2003, 2005) by a factor of about two indicates an increased occurrence of inflection points for cancerous vessels.

Conclusions

Phase tomography is a powerful approach for the analysis of the vascular network, down to the smallest capillaries. It is a label-free approach and does not suffer from artefacts originating from castings or stainings. The technique is non-destructive and therefore allows for subsequent histological analysis. The quantitative evaluation of vessel parameters revealed the absence of longer, oriented vessels within the tumor, compared to the surrounding healthy region.

Acknowledgements

The authors thank Michele Bernasconi and Zsofia Kovacs from the University Children's Hospital in Zurich for their support during animal experiments and

providing the mouse brain tumor sample and Irene Zanette from the Diamond Light Source and Georg Schulz from the Biomaterials Science Center in Basel for the support during beamtime. The authors also acknowledge the European Synchrotron Radiation Facility for the provision of beamtime at beamline ID19 under experiment number MD-860.

FUNDING

The financial contribution of the Swiss National Science Foundation (Project Nos. 144535 and 147172) is gratefully acknowledged.

Appendix

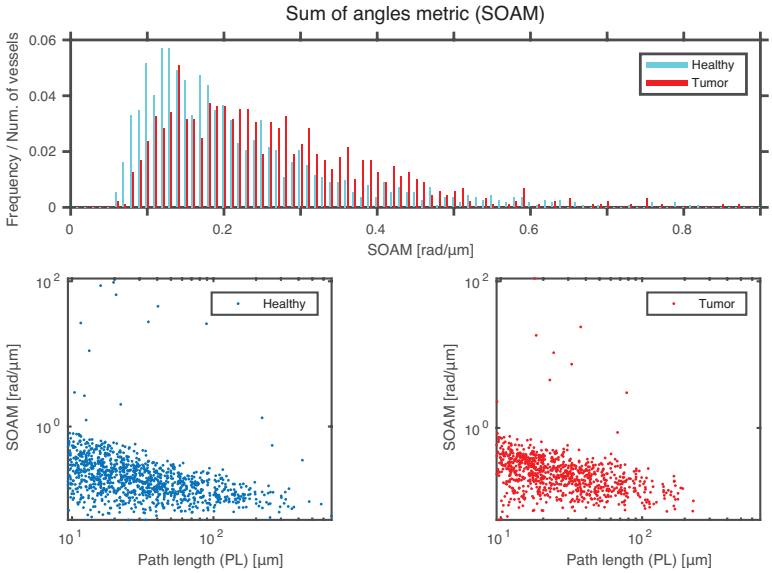

Figure 6: The histogram of SOAM (top) and the distribution plotted against path length for healthy tissue (left) and for cancerous tissue (right).

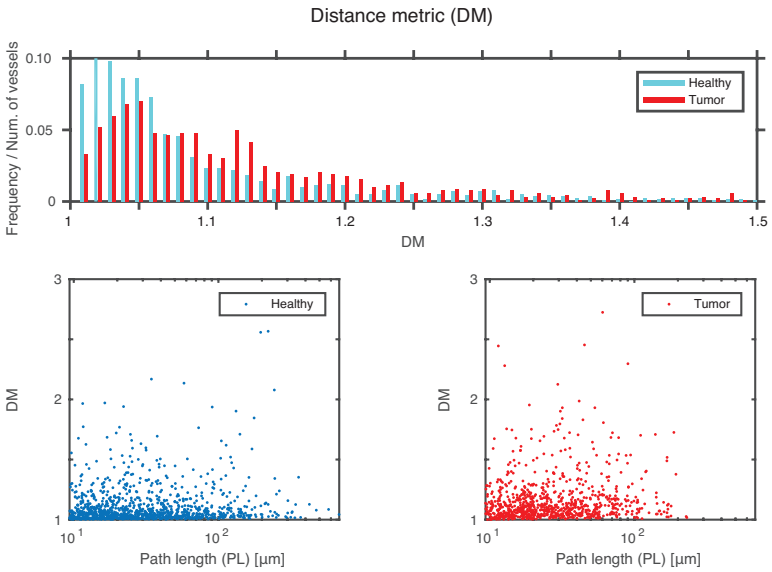

Figure 7: The histogram of DM(top) and the distribution plotted against path length for healthy tissue (left) and for cancerous tissue (right).

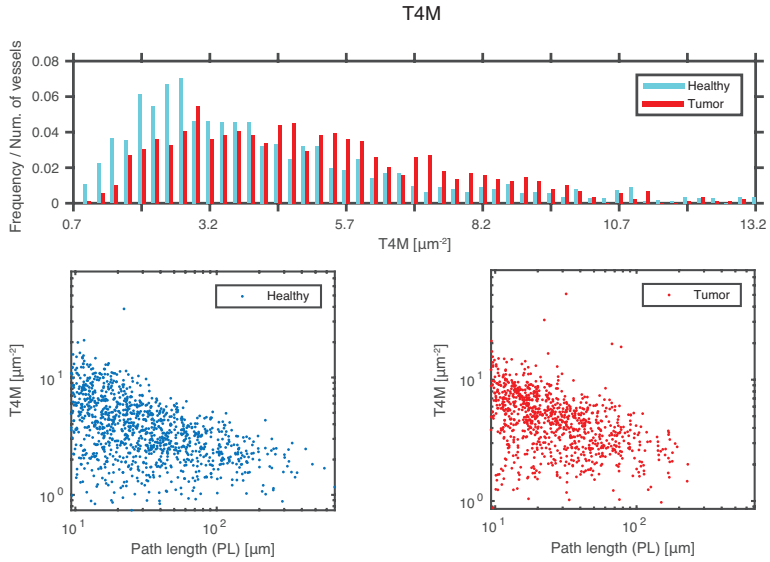

Figure 8: The histogram of T4M (top) and the distribution plotted against path length for healthy tissue (left) and for cancerous tissue (right).

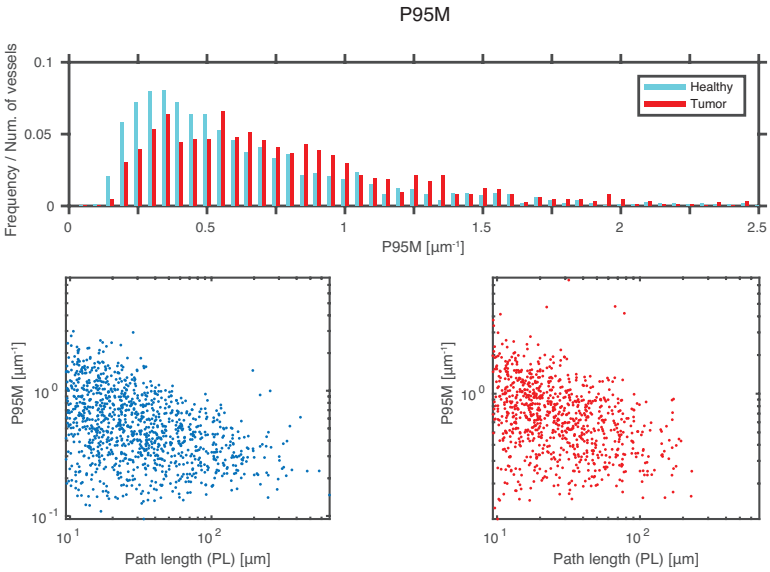

Figure 9: The histogram of P95M (top) and the distribution plotted against path length for healthy tissue (left) and for cancerous tissue (right).

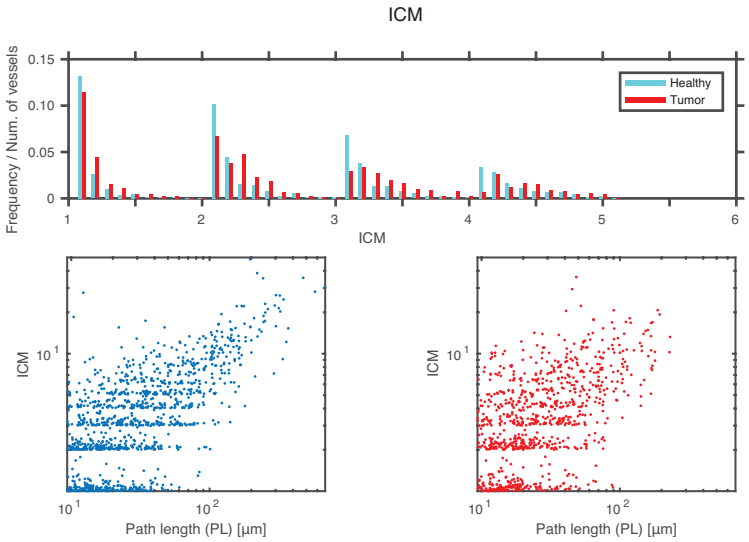

Figure 10: The histogram of ICM (top) and the distribution plotted against path length for healthy tissue (left) and for cancerous tissue (right).

References

Akslen, L.A., Straume, O., Geisler, S., Srlie, T., Chi, J.T., Aas, T., Brresen-Dale, A.L., Lnning, P.E., 2011. Glomeruloid microvascular proliferation is associated with lack of response to chemotherapy in breast cancer. British Journal of Cancer 105, 9–12.

Als-Nielson, J., McMorrow, D., 2011. Elements of Modern X-ray Physics (2nd Edition). John Wiley & Sons.

Beca, F., Polyak, K., 2016. Intratumor heterogeneity in breast cancer. Advances in Experimental Medicine and Biology 882, 69–89.

Bonse, U., Busch, F., 1996. X-ray computed microtomography (microCT) using synchrotron radiation (SR). Progress in Biophysics & Molecular Biology 65, 133–69.

Bullitt, E., Gerig, G., Pizer, S.M., Lin, W., Aylward, S.R., Sep 2003. Measuring tortuosity of the intracerebral vasculature from MRA images. IEEE transactions on medical imaging 22, 1163–71.

Bullitt, E., Zeng, D., Gerig, G., Aylward, S., Joshi, S., Smith, J.K., Lin, W., Ewend, M.G., October 2005. Vessel tortuosity and brain tumor malignancy: A blinded study. Academic radiology 12, 1232–40.

Burrell, R.A., McGranahan, N., Bartek, J., Swanton, C., September 2013. The causes and consequences of genetic heterogeneity in cancer evolution. Nature 501, 338–45.

Cai, Y., Wu, J., Li, Z., Long, Q., February 2016. Mathematical modelling of a brain tumour initiation and early development: A coupled model of glioblastoma growth, pre-existing vessel co-option, angiogenesis and blood perfusion. PLoS ONE 11, e0150296.

Cebulla, J., Kim, E., Rhie, K., Zhang, J., Pathak, A.P., Jul 2014. Multiscale and multi-modality visualization of angiogenesis in a human breast cancer model. Angiogenesis 17, 695–709.

Cloetens, P., 1999. Contribution to Phase Contrast Imaging, Reconstruction and Tomography with Hard Synchrotron Radiation. Ph.D. thesis. Vrije Universiteit Brussel, Belgium.

Douissard, P.A., Cecilia, A., Rochet, X., Chapel, X., Martin, T., van de Kamp, T., Helfen, L., Baumbach, T., Luquot, L., Xiao, X., Meinhardt, J., Rack, A., 2012. A versatile indirect detector design for hard X-ray microimaging. Journal of Instrumentation 7, P09016.

Folkman, J., Nov 1971. Tumor angiogenesis: therapeutic implications. The New England Journal of Medicine 285, 1182–6.

Frangi, A.F., Niessen, W.J., Vincken, K.L., Viergever, M.A., 1998. Multiscale vessel enhancement filtering. Springer Berlin Heidelberg, Berlin, Heidelberg. 130–7.

Friedmann-Morvinski, D., 2014. Glioblastoma heterogeneity and cancer cell plasticity. Critical reviews in oncogenesis 19, 327–36.

Gundersen, H.J.G., Mirabile, R., Brown, D., Boyce, R.W., 2013. Chapter 8 - stereological principles and sampling procedures for toxicologic pathologists. Haschek, W.M., Rousseaux, C.G., Wallig, M.A. (Eds.), Haschek and Rousseaux's Handbook of Toxicologic Pathology (Third Edition). third edition ed.. Academic Press, Boston, 215 –86.

Hieber, S.E., Bikis, C., Khimchenko, A., Schweighauser, G., Hench, J., Chicherova, N., Schulz, G., Müller, B., September 2016. Tomographic brain imaging with nucleolar detail and automatic cell counting. Scientific Reports 6, 32156.

ITK, 2017. The Insight Segmentation and Registration Toolkit (ITK). Available online at: http://www.itk.org.

Jain, R.K., Duda, D.G., Clark, J.W., Loeffler, J.S., Jan 2006. Lessons from phase III clinical trials on anti-VEGF therapy for cancer. Nature clinical practice. Oncology 3, 24–40.

Kak, A.C., Slaney, M., 1988. Principles of computerized tomographic imaging. IEEE Press.

Kikinis, R., Pieper, S.D., Vosburgh, K.G., 2014. 3D Slicer: A Platform for Subject-Specific Image Analysis, Visualization, and Clinical Support. Intraoperative Imaging and Image-Guided Therapy. Springer New York, 277–89.

Lang, S., Muller, B., Dominietto, M.D., Cattin, P.C., Zanette, I., Weitkamp, T., Hieber, S.E., Nov 2012. Three-dimensional quantification of capillary networks in healthy and cancerous tissues of two mice. Microvascular research 84, 314–22.

Lang, S., Zanette, I., Dominietto, M., Langer, M., Rack, A., Schulz, G., Le Duc, G., David, C., Mohr, J., Pfeiffer, F., Müller, B., Weitkamp, T., 2014. Experimental comparison of grating- and propagation-based hard X-ray phase tomography of soft tissue. Journal of Applied Physics 116, 154903.

Meacham, C.E., Morrison, S.J., September 2013. Tumour heterogeneity and cancer cell plasticity. Nature 501, 328–37.

Momose, A., May 2002. Phase-contrast X-ray imaging based on interferometry. Journal of Synchrotron Radiation 9, 136–42.

Müller, B., Fischer, J., Dietz, U., Thurner, P.J., Beckmann, F., 2006. Blood vessel staining in the myocardium for 3D visualization down to the smallest capillaries. Nuclear Instruments and Methods in Physics Research Section B: Beam Interactions with Materials and Atoms 246, 254 –61. Synchrotron Radiation and Materials Science.

Müller, B., Lang, S., Beckmann, F., Dominietto, M., Rudin, M., Zanette, I., Weitkamp, T., Rack, A., Hieber, S.E., 2012. Comparing the micro-vascular structure of cancerous and healthy tissues.

Nagy, J.A., Chang, S.H., Dvorak, A.M., Dvorak, H.F., Mar 2009. Why are tumour blood vessels abnormal and why is it important to know?

Paganin, D., Mayo, S.C., Gureyev, T.E., Miller, P.R., Wilkins, S.W., 2002. Simultaneous phase and amplitude extraction from a single defocused image of a homogeneous object. Journal of Microscopy 206, 33–40.

Pfeiffer, F., Bunk, O., David, C., Bech, M., Duc, G.L., Bravin, A., Cloetens, P., 2007. High-resolution brain tumor visualization using three-dimensional x-ray phase contrast tomography. Physics in Medicine and Biology 52, 6923.

Plouraboue, F., Cloetens, P., Fonta, C., Steyer, A., Lauwers, F., Marc-Vergnes, J.P., Aug 2004. X-ray high-resolution vascular network imaging. Journal of microscopy 215, 139–48.

Preim, B., Botha, C.P., 2013. Visual Computing for Medicine: Theory, Algorithms, and Applications. 2 ed., Morgan Kaufmann Publishers Inc., San Francisco, CA, USA.

Sato, Y., Nakajima, S., Shiraga, N., Atsumi, H., Yoshida, S., Koller, T., Gerig, G., Kikinis, R., June 1998. Three-dimensional multi-scale line filter for segmentation and visualization of curvilinear structures in medical images. Medical Image Analysis 2, 143–68.

Schneider, A., Thalmann, P., Pezold, S., Hieber, S.E., Cattin, P.C., 2015. Augmented reality assisted brain tumor extraction in mice. Lecture Notes in Computer Science 9254, 255–64.

Schulz, G., Weitkamp, T., Zanette, I., Pfeiffer, F., Beckmann, F., David, C., Rutishauser, S., Reznikova, E., Müller, B., 2010. High-resolution tomographic imaging of a human cerebellum: comparison of absorption and grating-based phase contrast. Journal of the Royal Society Interface 7, 1665–76.

Teague, M.R., Nov 1983. Deterministic phase retrieval: a green's function solution. Journal of the Optical Society of America 73, 1434–41.

Thalmann, P., Bikis, C., Hipp, A., Müller, B., Hieber, S.E., Schulz, G., 2017. Single and double grating-based X-ray microtomography using synchrotron radiation. Applied Physics Letters 110, 061103.

Thalmann, P., Bikis, C., Schulz, G., Dominietto, M.D., Rack, A., Schweighauser, G., Hieber, S.E., Müller, B., 2017. Multi-modal synchrotron radiation-based phase tomography for label-free brain imaging. in preparation.

Thalmann, P., Bikis, C., Schulz, G., Paleo, P., Mirone, A., Rack, A., Müller, B., 2017. Removing ring artifacts from synchrotron radiation-based hard x-ray tomography data. Proceedings of SPIE 10391.

TubeTK, 2017. The toolkit for the segmentation, registration, and analysis of tubes and surfaces in images. Available online at: http://www.tubetk.org.

Weitkamp, T., Diaz, A., David, C., Pfeiffer, F., Stampanoni, M., Cloetens, P., Ziegler, E., 2005. X-ray phase imaging with a grating interferometer. Optical Express 13, 6296–304.

Weitkamp, T., Haas, D., Wegrzynek, D., Rack, A., Jul 2011. *ANKAphase*: software for single-distance phase retrieval from inline X-ray phase-contrast radiographs. Journal of Synchrotron Radiation 18, 617–29.

3 Conclusions

The experimental data demonstrate that synchrotron radiation-based phase tomography is a powerful technique to visualize a mouse brain in a label-free manner. The contrast of the phase tomography techniques SDPR and XDGI was sufficient to resolve numerous anatomical microstructures within a mouse brain. To take advantage of the SDPR images, which exhibit a much higher spatial resolution than XDGI data, prominent ring artefacts had to be removed. The detection of individual cells and the segmentation of the smallest capillaries without employing any contrast agent was only possible using SDPR. The subsequent analysis of the segmented vascular network showed meaningful results for tortuosity measures and vascularization. Thus, we could demonstrate, that SDPR can depict angiogenesis of mouse brain tumors. Nevertheless, tomograms with an increased spatial resolution are expected to allow for a better distinction of the vascular network from the cell-dense surrounding tissue within the tumor.

Tumor segmentation can be tedious due to insufficient contrast or artifacts such as container-induced gradients. The complementarity of tomography modalities can be exploited to master these challenges and to improve the image analysis. More precisely, joint-histogram clustering based on registered data simplifies and improves tumor segmentation in comparison to thresholding, such that a tumor inside the brain can be localized with micrometer precision in a label-free manner.

From the increase in spatial resolution by a factor of two of XSGI with respect to XDGI, we can conclude that as long as the contrast in the XSGI tomograms is sufficient to recognize the anatomical microstructures of interest, XSGI is preferred over XDGI. Furthermore, as the analyzer grating is omitted, XSGI overcomes the limitation in spatial resolution present in XDGI. It should be noted, that simple optical magnification will only work to a limited extent, as deflection of X rays to neighbouring pixels causes phase wrapping artifacts. Finally, XSGI is a trade-off with respect to spatial resolution and quantitative characterization.

Bibliography

[1] K. A. McNeill, "*Epidemiology of Brain Tumors*", Neurologic Clinics, 34(4), 981–998 (2016).

[2] S.-P. Weathers and J. de Groot, "*VEGF Manipulation in Glioblastoma.*", Oncology (Williston Park, N.Y.), 29(10), 720–727 (2015).

[3] K. Seystahl, W. Wick, and M. Weller, "*Therapeutic options in recurrent glioblastoma–An update*", Critical Reviews in Oncology/Hematology, 99, 389–408 (2016).

[4] M. Niyazi, P. N. Harter, E. Hattingen, M. Rottler, L. von Baumgarten, M. Proescholdt, C. Belka, K. Lauber, and M. Mittelbronn, "*Bevacizumab and radiotherapy for the treatment of glioblastoma: brothers in arms or unholy alliance?*", Oncotarget, 7, 2313–2328 (2016).

[5] A. Krauth, R. Blanc, A. Poveda, D. Jeanmonod, A. Morel, and G. Székely, "*A mean three-dimensional atlas of the human thalamus: Generation from multiple histological data*", NeuroImage, 49(3), 2053–2062 (2010).

[6] B. Müller, J. Fischer, U. Dietz, P. J. Thurner, and F. Beckmann, "*Blood vessel staining in the myocardium for 3D visualization down to the smallest capillaries*", Nuclear Instruments and Methods in Physics Research Section B: Beam Interactions with Materials and Atoms, 246(1), 254–261 (2006).

[7] F. Plouraboué, P. Cloetens, C. Fonta, A. Steyer, F. Lauwers, and J.-P. Marc-Vergnes, "*X-ray high-resolution vascular network imaging.*", Journal of Microscopy, 215(2), 139–148 (2004).

[8] F. Pfeiffer, O. Bunk, C. David, M. Bech, G. Le Duc, A. Bravin, and P. Cloetens, "*High-resolution brain tumor visualization using three-dimensional x-ray phase contrast tomography*", Physics in Medicine and Biology, 52(23), 6923–6930 (2007).

[9] G. Schulz, T. Weitkamp, I. Zanette, F. Pfeiffer, F. Beckmann, C. David, S. Rutishauser, E. Reznikova, and B. Müller, "*High-resolution tomographic imaging of a human cerebellum: comparison of absorption and grating-based phase contrast*", Journal of the Royal Society Interface, 7(53), 1665–1676 (2010).

[10] D. T. Attwood, "*Soft X-Rays and Extreme Ultraviolet Radiation: Principles and Applications*", Cambridge University Press (1999).

[11] U. Bonse and F. Busch, "*X-ray computed microtomography (Î¼CT) using synchrotron radiation (SR)*", Prog. Biophys. Mol. Biol., 65(1), 133–169 (1996).

[12] A. Momose, "*Phase-contrast X-ray imaging based on interferometry*", Journal of Synchrotron Radiation, 9(3), 136–142 (2002).

[13] J. Als-Nielson and D. McMorrow, "*Elements of Modern X-ray Physics (2nd Edition)*", John Wiley & Sons (2011).

[14] A. Momose, "*Phase-sensitive imaging and phase tomography using X-ray interferometers*", Optics Express, 11(19), 2303–2314 (2003).

[15] S. Lang, I. Zanette, M. D. Dominietto, M. Langer, A. Rack, G. Schulz, G. Le Duc, C. David, J. Mohr, F. Pfeiffer, B. Müller, and T. Weitkamp, "*Experimental comparison of grating- and propagation-based hard X-ray phase tomography of soft tissue*", Journal of Applied Physics, 116(15), 154903 (2014).

[16] I. Zanette, M.-C. Zdora, T. Zhou, A. Burvall, D. H. Larsson, P. Thibault, H. M. Hertz, and F. Pfeiffer, "*X-ray microtomography using correlation of near-field speckles for material characterization*", Proceedings of the National Academy of Sciences of the United States of America, 112(41), 12569–12573 (2015).

[17] A. Momose and K. Hirano, "*The Possibility of Phase-Contrast X-Ray Microtomography*", Japanese Journal of Applied Physics, 38(S1), 625–629 (1999).

[18] Y. Chen, H. Guan, C. K. Hagen, A. Olivo, and M. A. Anastasio, "*Single-shot edge illumination x-ray phase-contrast tomography enabled by joint image reconstruction*", Optics Letters, 42(3), 619–622 (2017).

[19] I. Zanette, S. Lang, A. Rack, M. Dominietto, M. Langer, F. Pfeiffer, T. Weitkamp, and B. Müller, "*Holotomography versus X-ray grating interferometry: A comparative study*", Applied Physics Letters, 103(24), 244105 (2013).

[20] H. F. Talbot, "*LXXVI. Facts relating to optical science. No. IV.*", Philosophical Magazine, 9(56), 401–407 (1836).

[21] T. Weitkamp, C. David, C. Kottler, O. Bunk, and F. Pfeiffer, "*Tomography with grating interferometers at low-brilliance sources*", Proceedings of SPIE, 6318, 63180S (2006).

[22] K. Creath, "*Phase-measurement Interferometry Techniques*", Progress In Optics XXVI, E. Wolf, 26, 349–393 (1988).

[23] P. Cloetens, "*PhD thesis*", Vrije Universiteit Brussel, Belgium (1999).

[24] R. W. Gerchberg and W. O. Saxton, "*A practical algorithm for the determination of the phase from image and diffraction plane pictures*", Optik, 35, 237–246 (1972).

[25] A. Burvall, U. Lundström, P. A. C. Takman, D. H. Larsson, and H. M. Hertz, "*Phase retrieval in X-ray phase-contrast imaging suitable for tomography*", Optics Express, 19(11), 10359–10376 (2011).

[26] P. Cloetens, W. Ludwig, J. Baruchel, D. Van Dyck, J. Van Landuyt, J. P. Guigay, and M. Schlenker, "*Holotomography: Quantitative phase tomography with micrometer resolution using hard synchrotron radiation x rays*", Applied Physics Letters, 75(19), 2912–2914 (1999).

[27] D. Paganin, S. C. Mayo, T. E. Gureyev, P. R. Miller, and S. W. Wilkins, "*Simultaneous phase and amplitude extraction from a single defocused image of a homogeneous object*", Journal of Microscopy, 206(1), 33–40 (2002).

[28] M. R. Teague, "*Deterministic phase retrieval: a Green's function solution*", Journal of the Optical Society of America, 73(11), 1434–1441 (1983).

[29] F. Pfeiffer, O. Bunk, C. Kottler, and C. David, "*Tomographic reconstruction of three-dimensional objects from hard X-ray differential phase contrast projection images*", Nuclear Instruments and Methods in Physics Research Section A: Accelerators, Spectrometers, Detectors and Associated Equipment, 580(2), 925–928 (2007).

[30] A. Schneider, P. Thalmann, S. Pezold, S. E. Hieber*, and P. C. Cattin*, "*Augmented Reality Assisted Brain Tumor Extraction in Mice*", Lecture Notes in Computer Science, 9254, 255–264 (2015). *S. E. Hieber and P. C. Cattin shared last authorship.

[31] S. Lang, B. Müller, M. D. Dominietto, P. C. Cattin, I. Zanette, T. Weitkamp, and S. E. Hieber, "*Three-dimensional quantification of capillary networks in healthy and cancerous tissues of two mice.*", Microvascular Research, 84, 314–322 (2012).

[32] B. Müller, S. Lang, F. Beckmann, M. D. Dominietto, M. Rudin, I. Zanette, T. Weitkamp, A. Rack, and S. E. Hieber, "*Comparing the micro-vascular structure of cancerous and healthy tissues*", Proceedings of SPIE, 8506, 850607 (2012).

Acknowledgements

First of all I woud like to thank my „Dokorvater" Prof. Dr. Bert Müller for giving me the opportunity to do my PhD thesis at the Biomaterials Science Center, as well as for all the vivid and stimulating discussions helping to overcome the challenges faced. I also thank Dr. Simone Hieber for the supervision of my thesis and Prof. Dr. Sarah Köster for kindly acting as co-referee and for the evaluation of my thesis.

Special thanks goes to Dr. Georg Schulz for introducing me into the field of computed tomography, the many sleepless nights during beamtimes and for all the helpful discussions. Special thanks goes also to Dr. Christos Bikis for sharing his medical knowledge and the enormous help while writing the manuscripts, and his help with the development of the ring artifact removal algorithm.

Many thank goes also to Dr. Marco Dominietto for performing the animal experiment and his assistance during tumor analysis. I would like to express my gratitude to Dr. Adrian Schneider and Prof. Dr. Philippe Cattin making a precise tumor extraction feasible.

Sincere thanks goes to Dr. Felix Beckmann, Dr. Alexander Hipp, Dr. Julia Herzen and Dr. Imke Greving for their patience and continuous support during beamtimes at DESY and to Dr. Alexander Rack and Dr. Irene Zanette for their support at ESRF.

I also like to thank Prof. Dr. Michele Bernasconi and Dr. Zsofia Kovacs from the University Children's Hospital in Zurich for providing the tumor specimens and Gabriel Schweighauser and Dr. Jürgen Hench for providing the nerve specimen and their support during medical analysis as well as histology.

Many thanks goes also to Prof. Dr. Jörg Huwyler, Stefan Siegrist and Emre Cörek, for sharing their zebrafish data and the help during beamtime.

Furthermore, I would like to thank Pierre Paleo and Alessandro Mirone from ESRF for their help with the development of the ring artifact removal algorithm.

Special thanks goes to all the members of the Biomaterials Science Center for making the time during the thesis so enjoyable. It was a pleasure working with all of you.

Finally, I would like to express my profound gratitude to my friends and my parents, for always being there for me and always supporting me wherever they could. They always let me choose my own path and I'm extremely grateful for that. Most of all I'd like to thank Barbara, you are the love of my life and simply the best thing that ever happened to me. Thank you so much for everything. I love you.

Curriculum Vitae

Family Name:	Thalmann
First Name:	Peter
Citizenship:	Switzerland
Professional Address:	Biomaterials Science Center (BMC) University of Basel Gewerbestrasse 14 4123 Allschwil
Date of Birth:	03.11.1982
Place of Citizenship:	Bauma, ZH, Switzerland

Education

2013–2017	Doctor of philosophy (PhD) in experimental physics at University of Basel, Switzerland (Prof. B. Müller)
2006-2012	Master of Science Physics Swiss Federal Institute of Technology Zürich, Switzerland
2003–2005	Gymnasium Kantonale Maturitätsschule für Erwachsene Zürich, Switzerland
1998–2001	Commercial apprenticeship Gemeindeverwaltung Bauma, Switzerland

Professional Experience

2013–2017	PhD work at Biomaterials Science Center, University of Basel, Switzerland
2010-2012	Tutoring Physics Swiss Federal institute of technology Zürich, Swizterland
2001-2006	Employee Migrosbank Wallisellen, Switzerland